J. Fluid Mech. (2018), *vol.* 835, *pp.* 45–85.
doi:10.1017/jfm.2017.733

Turbulent flows over superhydrophobic surfaces: flow-induced capillary waves, and robustness of air–water interfaces

Jongmin Seo[1], Ricardo García-Mayoral[1,2] and Ali Mani[1,†]

[1]Center for Turbulence Research, Stanford University, Stanford, CA 94305, USA

[2]Department of Engineering, University of Cambridge, Cambridge CB2 1PZ, UK

(Received 6 January 2017; revised 24 August 2017; accepted 9 October 2017;
first published online 27 November 2017)

Superhydrophobic surfaces can retain gas pockets within their microscale textures when submerged in water. This property reduces direct contact between water and solid surfaces and presents opportunities for improving hydrodynamic performance by decreasing viscous drag. In most realistic applications, however, the flow regime is turbulent and retaining the gas pockets is a challenge. In order to overcome this challenge, it is crucial to develop an understanding of physical mechanisms that can lead to the failure of superhydrophobic surfaces in retaining gas pockets when the overlying liquid flow is turbulent. We present a study of the onset of failure in gas retention by analysing direct numerical simulations (DNS) of turbulent flows over superhydrophobic surfaces coupled with the deformation of air–water interfaces that hold the gas pockets. The superhydrophobic surfaces are modelled as periodic textures with patterned slip and no-slip boundary conditions on the overlying water flow. The liquid–gas interface is modelled via a linearized Young–Laplace equation, which is solved coupled with the overlying turbulent flow. A wide range of texture sizes and interfacial Weber numbers are considered in this study. Our analysis identifies flow-induced upstream-travelling capillary waves that are coherent in the spanwise direction as one mechanism for failure in retention of gas pockets. To confirm physical understanding of these waves, a semianalytical inviscid linear analysis is developed; the wave speeds obtained from the space–time correlations in the DNS data were found to match with the predictions of the semianalytical model. The magnitude of the pressure fluctuations due to these waves was found to increase with decreasing surface tension, and increase with a much stronger dependence on the slip velocity, when all numbers are reported in wall units. Based on a fitted scaling, a threshold criterion for the failure of superhydrophobic surfaces is developed that is based on estimates of the onset condition required for the motion of contact lines. The second contribution of this work is the development of boundary maps that identify stable and unstable zones in a parameter space consisting of working parameter and design parameters including texture size and material contact angle. We provide a brief description of previously identified failure modes of superhydrophobic surfaces, namely the stagnation pressure and shear-driven drainage mechanisms. In an overlay map, the stable and unstable zones due to each mechanism are presented. For various input conditions, we provide scaling laws that identify the most critical mechanism limiting the stability of gas retention by superhydrophobic surfaces.

† Email address for correspondence: alimani@stanford.edu

Key words: capillary waves, drag reduction, turbulent flows

1. Introduction

Among recent progress on developments of drag-reduction methods, the slip property of superhydrophobic surfaces has been highlighted for applications involving high-Reynolds-number hydrodynamic flows. Superhydrophobic surfaces can entrap a thin air layer on the surface, suggesting a remarkable potential for passive viscous drag reduction (Rothstein 2010; Golovin *et al.* 2016). Superhydrophobic surfaces are made of hydrophobic materials with roughness textures in a size range of nanometres to micrometres. When submerged in water, superhydrophobic surfaces hold gas bubbles in their roughness and preventing them from direct contact with water. This non-wetting state is called the Cassie–Baxter state (Cassie & Baxter 1944), which is in contrast to the Wenzel state, a fully wetted state where the liquid fills roughness elements (Wenzel 1936). In the Cassie–Baxter state, the contact area between solid and liquid is partially replaced by gas–liquid interfaces. Due to the low viscosity ratio of air to liquid (e.g. $\mu_{air}/\mu_{water} \approx 2\,\%$), flows over gas–liquid interfaces experience 'slippery' boundaries, which lead to a skin fiction reduction when compared to the conventional smooth, no-slip walls. Many experiments have utilized this slip effect and demonstrated drag reductions of more than 25 % in laminar flows (Ou, Perot & Rothstein 2004; Ou & Rothstein 2005; Choi & Kim 2006; Lee, Choi & Kim 2008; Lee & Kim 2009, 2011). Additional experiments further extended the drag-reduction capability of superhydrophobic surfaces to the turbulent flow regime. For boundary layers with fixed thickness and free-stream velocity, a given superhydrophobic surface is expected to achieve higher percentage drag reduction in the turbulent regime than in the laminar one due to the inner-versus-outer scale separation in turbulent flows, as discussed by Seo & Mani (2016). The flow regime associated with applications in most naval vehicles is indeed turbulent. Significant drag reductions of approximately 20 % have been measured in a variety of experiments on turbulent flows over superhydrophobic surfaces, consisting of either structured textures with regular arrays (Daniello, Waterhouse & Rothstein 2009; Woolford *et al.* 2009; Park, Sun & Kim 2014), or randomly distributed textures (Bidkar *et al.* 2014; Haibao *et al.* 2015; Srinivasan *et al.* 2015; Zhang *et al.* 2015; Rosenberg *et al.* 2016). Bidkar *et al.* (2014) and Ling *et al.* (2016) showed that when the surface textures have height variation, the resulting roughness in the overlying air–water interface can contribute to drag increase due to the form drag when the roughness size becomes on the order of the viscous sublayer.

Detailed analyses of turbulent flow fields have been carried out by numerical simulations that model the superhydrophobic surfaces as slip boundary conditions. DNS of turbulent flows over walls with a homogenized, prescribed slip length (Min & Kim 2004; Fukagata, Kasagi & Koumoutsakos 2006; Busse & Sandham 2012) investigated the effect of finite slip length on the overlying turbulent flows. Min & Kim (2004) identified that drag reduction was mainly gained by streamwise slip while any finite spanwise slip was found to lead to drag increase. Assuming that the homogenized slip length model is a valid model for textured superhydrophobic surfaces, Fukagata *et al.* (2006) presented a prediction model for drag reduction in terms of prescribed spanwise and streamwise slip lengths. More recently, DNS with

patterned slip boundary conditions resolved detailed surface geometry and investigated the effect of geometric parameters on turbulent flows over superhydrophobic surfaces. In these simulations, the slip length is a result of texture parameters such as gas fraction, texture spacing (Martell, Perot & Rothstein 2009; Martell, Rothstein & Perot 2010; Park, Park & Kim 2013; Jelly, Jung & Zaki 2014; Türk *et al.* 2014; Lee, Jelly & Zaki 2015; Rastegari & Akhavan 2015; Seo, García-Mayoral & Mani 2015; Seo & Mani 2016), or texture height (Jung, Choi & Kim 2016). These studies indicate that slip lengths achieved under turbulent flows are different from nominal slip lengths that are obtained from Stokes flow analyses, which are solely functions of surface geometry. More recently, Seo & Mani (2016) presented a scaling relation predicting the slip length under turbulent flows for a wide range of texture size. They found that when the texture size is small compared to the overlying turbulent eddies, the slip length is independent of the overlying flow, consistent with Stokes flow solutions. However, in the large-texture limit, the slip length was found to decrease with flow velocity to the two-thirds power (Seo & Mani 2016). In the latter case, they found that homogenized slip boundary conditions are inappropriate representatives of the effects of patterned boundaries.

While kinematics of flows over superhydrophobic surfaces are widely investigated, only a few investigations have studied the mechanism of gas bubble depletion under turbulent flows, even though gas depletion is a critical bottleneck towards real applications. In reality, superhydrophobic surfaces exposed to turbulent boundary layers increase drag if the surfaces lose their gas bubbles under high shear and pressure fluctuations (Aljallis *et al.* 2013). As a result, successful drag reductions reported by experiments are limited to less than 30 % (Daniello *et al.* 2009; Woolford *et al.* 2009; Bidkar *et al.* 2014; Haibao *et al.* 2015; Srinivasan *et al.* 2015; Zhang *et al.* 2015; Rosenberg *et al.* 2016). Most previous computational studies assumed flat gas–liquid interfaces and a stable Cassie–Baxter state under infinite surface tension; these idealized assumptions inevitably result in unrealistically large drag reductions, often more than 50 %. Under a static pressure, Patankar (2010) discussed two causes of interface breakup: de-pinning transition, which occurs when the microscopic contact angle at the corner of the roughness is larger than its threshold; and sag transition, which occurs when a curved interface touches the bottom of roughness. Li, Alame & Mahesh (2017) analytically and computationally studied the effect of gas–liquid interface on drag reduction, resolving texture spacing and height in laminar channel flow over superhydrophobic surfaces. Considering laminar flow regimes, Wexler, Jacobi & Stone (2015*b*) identified the shear-driven drainage mechanism as a failure mode for drag reduction by slippery surfaces. They found that when texture grooves are longer than a threshold length, the streamwise pressure difference due to the imposed shear on a lubricant fluid can overcome the stabilizing surface tension force and lead to drainage of lubricant from the surface. A similar mechanism can lead to drainage of air bubbles from superhydrophobic surfaces in both the laminar and turbulent regimes. However, as we shall see, the thresholds are significantly higher in this case since air bubbles, due to their low viscosity, are exposed to much lower shear compared to slippery lubricants. The first study on the failure mechanisms of superhydrophobic surfaces in turbulent flows was introduced in Seo *et al.* (2015) by investigating averaged pressure fields from DNS data. Seo *et al.* (2015) demonstrated that the stagnation of slip flows encountering roughness elements can pressurize the gas–liquid interface, eventually leading a transition to the Wenzel state, when texture size becomes large compared to near-wall eddies. The deleterious effect on plastron stability by increasing texture size is consistent with a theoretical analysis by Piao &

Park (2015) that considered unsteady pressure fluctuations on the gas–liquid interface in a superhydrophobic surface. However, in the analysis by Seo *et al.* (2015) the interface deformation was studied as a postprocessing of pressure data obtained from DNS of turbulence on superhydrophobic textures with a flat interface. More accurate analysis requires investigations of direct coupling between the two effects, where one also considers the dynamic influence of interface deformation on the overlying flow.

In this paper, we investigate DNS of turbulent flows over superhydrophobic surfaces while direct dynamic coupling between flow and interface deformation is simulated via solutions to the Young–Laplace equation. We reveal that such coupling can lead to a new failure mechanism, which we refer to as flow-induced capillary waves. For the purpose of this investigation we conducted DNS of turbulent channel flows over superhydrophobic surfaces considering a wide range of texture size. The motion of the gas–liquid interface is modelled via realtime coupled linearized boundary conditions considering a wide range of Weber numbers. The failure onset is defined by the conditions required for the initiation of motion of the contact line. By considering a broad range of input parameters, the scaling laws of flow-induced capillary waves and the resulting failure onsets are developed and verified. In this way we analyse the effect of flow and interfacial parameters on the depletion of gas bubbles.

The first objective of our investigation is to determine whether dynamic turbulence-interface coupling can result in any effect on flow statistics, most importantly on drag reduction. While bent meniscus shapes due to pressure differences between trapped gas bubbles and overlying liquid have been observed in many experiments for laminar flows (Byun *et al.* 2008; Tsai *et al.* 2009; Karatay *et al.* 2013; Xue *et al.* 2015), the effect of interface deformation on turbulent flows has often been ignored in many computational studies that assumed flat interfaces (Martell *et al.* 2009, 2010; Park *et al.* 2013; Jelly *et al.* 2014; Türk *et al.* 2014; Rastegari & Akhavan 2015; Seo *et al.* 2015; Jung *et al.* 2016; Seo & Mani 2016). In laminar flows, the bubble deformation significantly impacts the slip property shown by theory (Davis & Lauga 2009), experiments (Karatay *et al.* 2013), and numerical simulations (Steinberger *et al.* 2007; Hyväluoma & Harting 2008; Teo & Khoo 2010, 2014). Steinberger *et al.* (2007) demonstrated that the protrusion angle of the gas bubbles, an angle created by a solid element, liquid, and gas pocket, can change a slippery surface to a sticky surface even in the Cassie–Baxter state. In agreement with Steinberger *et al.* (2007), Hyväluoma & Harting (2008) showed that the slip length is maximized when the gas–liquid interface is flat, and it can be negative when the interface protrudes into the liquid. Karatay *et al.* (2013) experimentally controlled a bubble shape by changing pressure in the gas layer and reported that the slippage was a function of meniscus curvature. Although the magnitude of deformation is expected to be small in the air–water interfaces on superhydrophobic surfaces (Martell *et al.* 2010), fully coupled turbulent flow simulations with dynamics of the interface should be conducted to examine the outcome of the interaction. Beyond the impact on the performance, interface deformation can critically affect the stability of the gas pockets.

As the second objective of this study, we investigate the onset mechanism of interface breakage as texture size and Weber number increase, leading to the loss of the drag-reducing effect. We characterize the dependence of the flow-induced capillary waves on texture size and Weber number, and thereby suggest a failure onset by considering the pressure required to initiate the motion of contact lines from their approximate pinned condition.

The paper is organized as follows. In § 2 we present the governing equations, including dynamics associated with flows as well as the gas–liquid interface, and

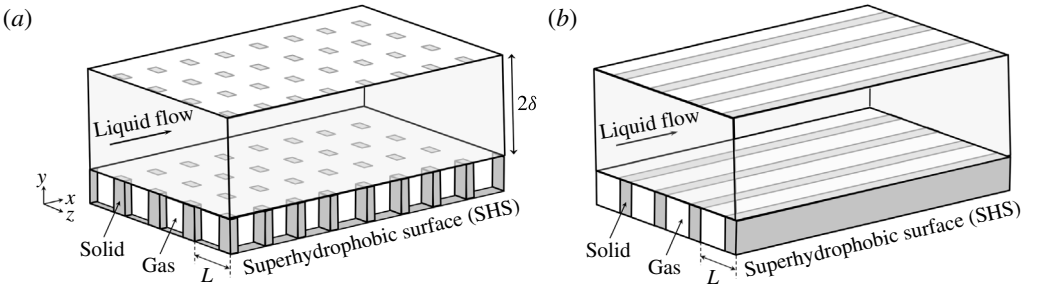

FIGURE 1. Schematic representation of a channel flow with superhydrophobic surfaces on both top and bottom walls: (*a*) isotropic posts (*b*) streamwise ridges.

discuss the key dimensions and dimensionless parameters for the problem. In § 3, algorithms and computational details to numerically solve the set of equations are presented. The DNS results of our simulations are presented and discussed in § 4. A semianalytical model for the capillary waves appearing in the gas–liquid interface is proposed and compared with DNS data in § 5. In § 6, we present scaling laws for dynamic characteristics and fluctuations of capillary pressure. Section 7 provides a boundary map indicating the stable and unstable zones of operation of superhydrophobic surfaces under turbulent flow conditions. Specifically, we provide quantitative comparison with the previously identified failure mechanisms, namely the stagnation pressure mechanism and shear-driven drainage mechanism, and provide conditions determining the most critical mode of failure in terms of input parameters. Finally, our discussion and conclusions are summarized in § 8.

2. Problem formulation

We study the turbulent liquid flow in a periodic channel enclosed with superhydrophobic walls that entrap gas pockets, as sketched in figure 1. The periodic roughness structure is defined by its width, w, and period, L, as shown in figure 2(*a*). We consider the incompressible Navier–Stokes equations for fluid flow,

$$\boldsymbol{\nabla}\cdot\boldsymbol{u}=0, \tag{2.1}$$

$$\frac{\partial \boldsymbol{u}}{\partial t}+\boldsymbol{u}\cdot\boldsymbol{\nabla}\boldsymbol{u}=-\boldsymbol{\nabla}p+\nu\nabla^2\boldsymbol{u}, \tag{2.2}$$

where ν is the kinematic viscosity of liquid and the pressure p is normalized by the liquid density.

In the channel, both top and bottom walls are superhydrophobic surfaces with periodic solid roughness elements and gas pockets fully trapped in between the roughness elements. We assume no-slip on the solid surface and free shear on gas–liquid interface. The imposed shear-free boundary condition on the gas–liquid interface is

$$\frac{\mathrm{d}u}{\mathrm{d}y}+\frac{\mathrm{d}v}{\mathrm{d}x}=0,\quad \frac{\mathrm{d}w}{\mathrm{d}y}+\frac{\mathrm{d}v}{\mathrm{d}z}=0. \tag{2.3a,b}$$

This ideal free-shear condition is standard in the literature for DNS of turbulent flows over superhydrophobic surfaces considering a low viscosity ratio of air to water

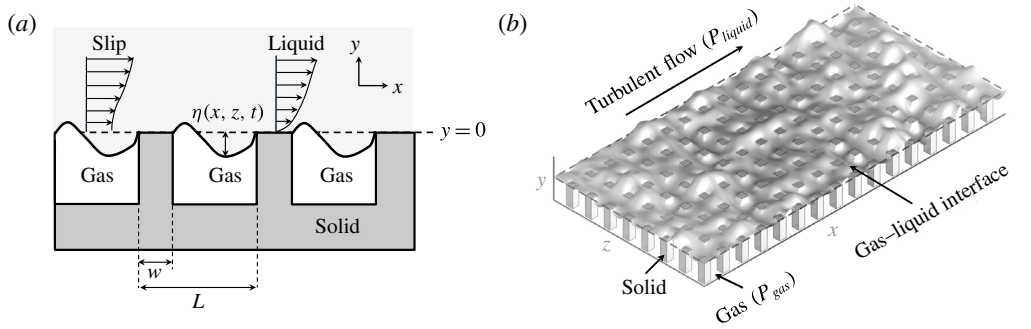

FIGURE 2. (*a*) Schematic of patterned slip and no-slip boundary conditions at superhydrophobic surfaces with deformable interfaces. The interface location is defined as η, which is the vertical distance from the wall plane. (*b*) Gas–liquid interface on solid posts. For both figures, the baseline wall location ($y = 0$) is denoted by dashed lines.

(Martell *et al.* 2009, 2010; Park *et al.* 2013; Jelly *et al.* 2014; Türk *et al.* 2014; Lee *et al.* 2015; Seo *et al.* 2015; Seo & Mani 2016). We assume a sufficiently large texture depth and we do not resolve the texture height. Schönecker, Baier & Hardt (2014) examined the ideal free-shear assumption in flows over superhydrophobic surfaces and showed this treatment to be essentially correct for the air–water system if the texture height is larger than a threshold comparable to L. We consider the wall-normal velocity terms in (2.3) since the interface is allowed to deform so that the wall-normal velocity on the wall, $v(y = 0)$, can be non-zero. We assume viscous effects from the gas layer are negligible (see appendix A).

We define η as the interface height, measured from the plane that contains the no-slip, flat top of the posts, $y = 0$, as sketched in figure 2. The deformation of the interface is obtained via the linearized Young–Laplace equation,

$$\nabla^2 \eta \approx \frac{P_{liquid} - P_{gas}}{\sigma}, \tag{2.4}$$

where σ is the surface tension. Within the gas pockets, we assume P_{gas} is uniform, and governed by the mass conservation of the gas,

$$\iint \eta \, \mathrm{d}x \, \mathrm{d}z = 0. \tag{2.5}$$

The gas–liquid interface is assumed to be effectively pinned to the post edges, as in figure 2. The pinned interface assumption is widely adopted in simulations of flows over superhydrophobic surfaces with curved interfaces (Steinberger *et al.* 2007; Hyväluoma & Harting 2008; Teo & Khoo 2010, 2014; Seo *et al.* 2015). As discussed by Seo *et al.* (2015), the pinned assumption is an asymptotic model for a contact line moving on a round corner, in the limit that the corner radius is much smaller than L, and the microscopic contact angle is within the advancing and receding contact angles.

We assume that η is small, and model its fluctuations through a linearized boundary condition for the wall-normal velocity at $y^+ = 0$. The motion of the interface generates a non-zero wall-normal velocity at the interface,

$$v(x, y = \eta, z, t) = \frac{\mathrm{D}\eta}{\mathrm{D}t} = \frac{\partial \eta}{\partial t} + u\frac{\partial \eta}{\partial x} + w\frac{\partial \eta}{\partial z}. \tag{2.6}$$

The Taylor expansion of (2.6) at $y=0$, combined with the continuity equation, leads to

$$v(x, y=0, z, t) = \frac{\partial \eta}{\partial t} + \frac{\partial(\eta u)}{\partial x} + \frac{\partial(\eta w)}{\partial z}. \tag{2.7}$$

This non-zero wall-normal velocity is imposed as a boundary condition for the overlying, turbulent, liquid flow. The validity and outcome of linearization of the boundary conditions is discussed in appendix B.

2.1. *Dimensionless parameters*

In this problem we consider three key dimensionless parameters on scales relevant to turbulence, superhydrophobic surfaces, and surface tension of the gas–liquid interface. The first dimensionless parameter is the friction Reynolds number $Re_\tau = u_\tau \delta/\nu$, which measures the separation of length scales from the boundary layer thickness, δ, to the viscous unit length $\delta_\nu = \nu/u_\tau$, where u_τ is the friction velocity defined by $\sqrt{\tau_w/\rho}$ and τ_w is wall shear stress. τ_w is the mean shear averaged over the entire interface area (including solid zones and shear-free air zones). This mean shear can be computed from the mean pressure gradient, using a momentum balance leading to $2\tau_w = (\overline{\mathrm{d}p}/\mathrm{d}x)(2\delta)$. In this work we run our simulations at $Re_\tau \approx 200$–400. These Reynolds numbers are much lower than realizable numbers in practical applications for naval applications, typically $Re_\tau \gtrsim 4000$; for example, a free-stream velocity of $\sim$5 m s^{-1} over a plate $\sim$1 m long.

However, since superhydrophobic surfaces only modify the inner region of turbulent wall-bounded flows, their effects can be studied using low $Re_\tau \approx 180$–200 as long as the dimensionless quantities based on the inner scale match the application of interest (Martell *et al.* 2010; Seo *et al.* 2015). Martell *et al.* (2010) first showed that the mean velocity profiles with two different Re_τ are collapsed when L^+ is fixed. Seo *et al.* (2015) showed that the effects of superhydrophobic surfaces on turbulent flows are confined to the near-wall region, $y^+ \lessapprox 80$, as long as the superhydrophobic surface texture scale is smaller than the outer scale of the flow. They concluded that this modification to the inner region of the flow can be captured insensitive to the Reynolds number down to $Re_\tau \approx 200$. Increasing Reynolds number only modifies the outer flow in the same fashion as in the boundary layer over a smooth wall. In other words, the Reynolds number effects can be captured well by extending the log-layer in turbulent wall-bounded flows.

Another important dimensionless parameter is the size of the texture in viscous units $L^+ = L/\delta_\nu$, a measure of how large the texture is compared to the near-wall eddies. Many computational (Martell *et al.* 2010; Park *et al.* 2013; Türk *et al.* 2014; Lee *et al.* 2015; Rastegari & Akhavan 2015; Seo *et al.* 2015; Seo & Mani 2016) and experimental (Daniello *et al.* 2009; Park *et al.* 2014) investigations show that the slip length, and thus drag reduction, increase with larger L^+ when the solid fraction is fixed. Seo & Mani (2016) showed that the slip length followed a linear scaling of texture size, and matched with the analytical solution from Stokes flow (Ybert, Barentin & Cottin-Bizonne 2007; Davis & Lauga 2010) that obtained from the same geometry, when texture size in wall units is smaller than approximately 10 for isotropic posts. When the texture size becomes larger, the slip length in wall units increases nonlinearly with a scaling exponent less than 1 (Park *et al.* 2013; Türk *et al.* 2014; Rastegari & Akhavan 2015; Seo & Mani 2016). For small L^+, flows with superhydrophobic surfaces preserve the behaviour of canonical smooth-wall flows,

while for large L^+ the effect of superhydrophobic surfaces completely disrupts the buffer layer, similar to the behaviour of flows over rough walls. Recent DNS (Türk *et al.* 2014; Rastegari & Akhavan 2015; Seo *et al.* 2015) reached L^+ down to the size relevant to practical applications $L^+ \approx 6$–8, comparable to typical experimental values of the texture period $L^+ \approx 0.5$–5 (Daniello *et al.* 2009; Woolford *et al.* 2009; Park *et al.* 2014). In the present work, we have investigated textures with sizes $L^+ \approx 13$–155, where the smallest texture size is close to the realistic texture size. Texture size on the order of hundreds is not considered in our study since the gas pockets would be destroyed due to high momentum of turbulent shear and slip flows.

Another texture-related dimensionless parameter is the solid fraction, which is equal to $\phi_s = w^2/L^2$ in the case of isotropic posts. This parameter is typically in the range 10 %–20 % and does not vary by an order of magnitude. In the present study we considered $\phi_s = 1/9$, which is in the range of practical scenarios. We considered one case for a streamwise ridge with a solid fraction of $\phi_s = w/L = 1/3$.

The last dimensionless number is the Weber number, which measures the relative importance of the surface tension to the momentum. Using inner scalings, Weber number could be defined as $We^+ = \rho u_\tau^2 \delta_\nu / \sigma$. Noting $u_\tau \delta_\nu = \nu$, this parameter can be also presented as a Capillary number $We^+ = Ca^+ = \mu u_\tau / \sigma$. When discussing the DNS results, we will use an alternative Weber number defined based on the texture size, $We_L = \rho u_\tau^2 L/\sigma = We^+ L^+$. In our simulations we use $We_L = 10^{-3}$–8×10^{-3}. Another Weber number can be defined based on the slip velocity, U_s, as $We_s = \rho U_s^2 L/\sigma$. We will show that this definition leads to collapse of data related to the flow-induced capillary waves. However, since We_s is not known *a priori*, we prefer to keep We_L (or We^+) as an input dimensionless parameter, and to provide explicit relations leading to We_s after investigating DNS data.

In § 7, we will discuss the parameter space and regions of stable design. In this case, it is beneficial to use We^+ as the dimensionless parameter instead of We_L. This is because We^+ is solely dependent on the imposed flow, and independent of superhydrophobic surface design choices (e.g., L^+ and advancing and receding contact angles). For channel flows with a prespecified pressure gradient, u_τ is known *a priori* and so is We^+. For boundary layers, U_∞ is known instead of u_τ, and thus We^+ is not exactly independent of texture parameters. As a useful rough approximation, however, one can write We^+ in terms of the free-stream velocity as $We^+ \simeq \mu U_\infty/(25\sigma)$. This approximation can be justified given that the ratio U_∞/u_τ is in the range 22–30 in boundary layers over practical ranges of Reynolds numbers, $Re_\tau \approx 1000$–$20\,000$, with a weak logarithmic dependence on the Reynolds number. In situations with slip velocity, one can use the shifted-TBL model (Seo & Mani 2016) and find that the same approximation holds as long as drag reduction is much less than the drag itself. In other words, in a design problem, a reasonable approximation of We^+ is available prior to the decision on the design details, while one can easily improve on these approximations *a posteriori* via algebraic relations provided for the shifted-TBL model and slip length in Seo & Mani (2016). These small corrections are expected to converge very rapidly with a small number of iterations.

In § 7 we will discuss additional parameters relating to design, including the advancing contact angle, which is related to the surface chemistry and determines the onset of failure. Another design consideration is the use of barriers in between the texture grooves to keep air regions in the form of isolated pockets. However, for the majority of the paper, where the physics of flow-induced capillary waves are discussed, we only need L^+ and We^+ as the key controlling parameters.

Case	Surface type	L^+	We_L ($\times 10^{-3}$)	Re_τ	D_x^+	D_z^+	$N_x \times N_z \times N_y$	DR (%)
P13W8	Posts	12.93	8	197.5	1240.9	620.5	$1152 \times 576 \times 128$	13
P26W4	Posts	25.85	4	197.5	1240.9	620.5	$576 \times 288 \times 128$	36
P26W8	Posts	25.85	8	197.5	1240.9	620.5	$576 \times 288 \times 128$	36
P39W2	Posts	38.78	2	197.5	1240.9	620.5	$768 \times 384 \times 128$	42
P39W4	Posts	38.78	4	197.5	1240.9	620.5	$768 \times 384 \times 128$	42
P78W1	Posts	77.56	1	197.5	1240.9	620.5	$384 \times 192 \times 128$	55
P78W2	Posts	77.56	2	197.5	1240.9	620.5	$384 \times 192 \times 128$	55
P78W4	Posts	77.56	4	197.5	1240.9	620.5	$384 \times 192 \times 128$	55
P78W5	Posts	77.56	5	197.5	1240.9	620.5	$384 \times 192 \times 128$	55
P155W1	Posts	155.1	1	197.5	2481.9	620.5	$384 \times 192 \times 128$	69
P155W2	Posts	155.1	2	197.5	1240.9	620.5	$192 \times 192 \times 128$	69
P155W4	Posts	155.1	4	197.5	1240.9	620.5	$192 \times 192 \times 128$	69
P155W2$_{Re}$	Posts	155.1	2	395.0	2481.9	1240.9	$384 \times 384 \times 192$	69
R155W2	Ridges	155.1	2	197.5	1240.9	620.5	$192 \times 192 \times 128$	59

TABLE 1. Simulation parameters. L^+ is the pattern spacing, We_L is Weber number based on L and u_τ, and Re_τ is the friction Reynolds number. Domain size in viscous units is D_x^+ and D_z^+ for the streamwise and spanwise directions, respectively. The number of grid points is N_x, N_z, and N_y, for streamwise, spanwise, and wall-normal directions respectively. The grid size is given by the computational domain size and number of grid points. DR is the drag reduction obtained by $DR = (C_{f,smooth} - C_{f,SHS})/C_{f,smooth}$, where SHS stands for superhydrophobic surface.

3. Numerical method

The Navier–Stokes equations are numerically discretized and solved with the code of Seo *et al.* (2015), modified to simulate a deformable interface on superhydrophobic surfaces. In each time step, the motion of turbulent flow is fully coupled with the Young–Laplace equation and the kinematic conditions on the interface. The code uses the second-order finite-difference scheme on a staggered, Cartesian mesh with a uniform grid size in the streamwise (x) and spanwise (z) directions, and a non-uniform grid-size in the wall-normal (y) direction (Morinishi *et al.* 1998). The time discretization scheme for liquid flow is the second-order Adams–Bashforth method. The domain size is $2\pi\delta \times \pi\delta \times 2\delta$ in the streamwise, spanwise and wall-normal directions, respectively. All simulations were run under a constant mean pressure gradient condition, which ensured fixed Re_τ and thereby predefined L^+. We mainly use $Re_\tau \approx 200$ for computational cost and add one simulation at $Re_\tau \approx 400$ to examine the Reynolds number dependence. We study two types of pattern geometries with a finite period L sketched in figure 1(a), isotropically distributed posts, and figure 1(b), streamwise-aligned ridges. The width of the pattern is fixed to $w = L/3$, which leads to a 1/9 solid fraction for isotropic posts and a 1/3 solid fraction for streamwise ridges. All simulation parameters are summarized in table 1. Though not specified, results with a flat interface ($We^+ = 0$) from Seo *et al.* (2015) are used.

The spatial resolution in the wall-parallel direction is restricted by texture size, as even the grid size for the largest texture is finer than the resolution requirement for DNS of turbulent flows, $\Delta x^+ \approx 6.4$, $\Delta z^+ \approx 3.2$. The non-uniform grid in the wall-normal direction has a minimum size $\Delta y^+ = 0.15$ at the wall, and a maximum $\Delta y^+ = 12$ at the centre of the channel. The grid resolutions and the number of grid points per texture period are sufficient to provide grid-converged statistics with finer resolutions

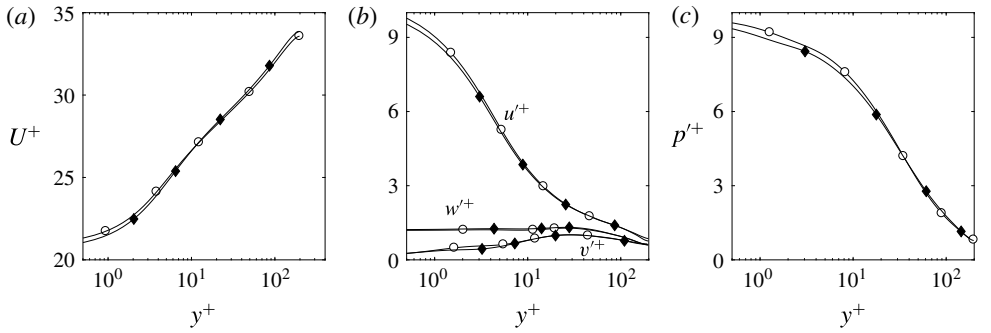

FIGURE 3. Comparison of statistics for post geometries at $L^+ \approx 155$, $Re_\tau \approx 200$, and $We_L = 2 \times 10^{-3}$. (*a*) Mean streamwise velocity profile; (*b*) velocity r.m.s. fluctuations; (*c*) pressure r.m.s. fluctuations. –○–, posts with $\Delta x^+ = 6.4$, $\Delta z^+ = 3.2$ –◆–, posts with $\Delta x^+ = 3.2$, $\Delta z^+ = 1.6$.

within 1 % error, when the interface is flat. We have conducted a resolution test for a simulation with a deformable interface at $L^+ \approx 155$, $Re_\tau \approx 200$, and $We_L = 2 \times 10^{-3}$ and the results showed grid-converged statistics. Specifically, for this case we refined the computational mesh from $\Delta x^+ = 6.4$, $\Delta z^+ = 3.2$ to $\Delta x^+ = 3.2$, $\Delta z^+ = 1.6$. Figure 3 confirms that the velocity statistics are not affected by the change in grid size. Specifically, the mean flow rate was within 0.7 % difference between the two calculations and the slip velocity was within 0.8 % difference. The wavelength of capillary waves obtained by space–time correlations showed grid-converged results within 4 % error.

On gas–liquid interfaces, the coupling among pressure $p_i(x, z, t)$, velocity at the gas–liquid interface, $\boldsymbol{u}_i(x, z, t)$, and deformation of interface, $\eta(x, z, t)$, is resolved explicitly using the second-order Adams–Bashforth scheme consistent with that used for the overlying flows, where the subscript i denotes the location at the first computational cells right above the interface. The first step for the coupling is to advance the interface location through (2.7),

$$\eta^{n+1} = \eta^n + \Delta t \left(\frac{3}{2} \left(v_i^n - \frac{\partial (\eta u_i)^n}{\partial x} - \frac{\partial (\eta w_i)^n}{\partial z} \right) - \frac{1}{2} \left(v_i^{n-1} - \frac{\partial (\eta u_i)^{n-1}}{\partial x} - \frac{\partial (\eta w_i)^{n-1}}{\partial z} \right) \right), \tag{3.1}$$

where the superscript 'n' denotes the information at the current time step, '$n+1$' denotes the information at the next time step, and '$n-1$' denotes the information at the previous time step. The spatial discretization of (3.1) is a second-order finite-difference scheme. The resulting η^{n+1} is used in the Young–Laplace equation, equation (2.4), to find the pressure in the cells right above the interface, $p_i^{n+1} = \sigma \nabla^2 \eta^{n+1}$. Then p_i^{n+1} is used as boundary conditions in the Poisson system for continuity of the overlying fluid equations, $\nabla^2 p^{n+1} = \nabla \boldsymbol{u}^{(n+1/2)} / \Delta t$, in which $\boldsymbol{u}^{(n+1/2)}$ is the intermediate velocity fields before the projection in the fractional step method (Kim & Moin 1985). In this case, solving the Poisson system satisfies continuity of the overlying fluid, except for the cells right above the interface. For those cells, instead of solving the Poisson system, continuity is satisfied by determining the v-component of the velocity on the interface. The wall-normal velocity determined in

this way, v_i^{n+1}, is used to advance interface deformation in the next time step in (3.1). The implementation of this coupling in the code is verified through an analytical solution of the perturbation problem under uniform velocity, in which one wall is fully covered by an initially perturbed gas–liquid interface with finite surface tension. The code verification against the analytical solution is confirmed by matching the time frequency of a single spatial wave mode as well as the corresponding velocity and pressure fields. Details of this verification are described in appendix C.

Fast Fourier transform (FFT) of the Poisson system in periodic directions can be exploited to significantly save the computational cost by forming a tri-diagonal matrix system, $(-k_x^2 - k_z^2 + \partial_y^2)\widehat{p}^{n+1} = \widehat{S}$, where $\widehat{p}$ is the Fourier transformed pressure fields, (k_x, k_z) are the modified wavenumbers for spatial discretization operators in x and z direction, and $\widehat{S}$ is the Fourier transformed right-hand side of the Poisson system (Kim & Moin 1985). However, the above-mentioned coupled algorithm results in an inhomogeneous boundary treatment for the Poisson system since the treatment on the gas–liquid interface is different from those on solid–liquid boundaries, i.e. on posts. This prevents us from taking advantage of FFT when solving the Poisson system. To remedy this, we model the solid texture using a method consistent with the air–water interface. Specifically, we assumed very high but finite stiffness for the solid post in the y-direction. The solid stiffness is selected to be much larger than any other stiffness in the system, and we have verified independence of the DNS result from the choice of stiffness by comparing statistics of turbulent channel flows over the wall with finite stiffness against a smooth-wall channel of Moser, Kim & Mansour (1998). Over the solid posts, the non-deformation of the boundary is imposed such as

$$P_{solid} \approx k_s \eta, \tag{3.2}$$

where k_s is the artificial spring constant, $k_s^+ = k_s/(\rho {u_\tau}^2/\delta_v) = 4000$, chosen so that both the interface deformation and its time derivative remain negligible, $\eta_{max}^+ = 0.005$ and $v_{y=0,max}^+ = 0.003$. Both values are much smaller than deformations observed in the gas–liquid interface. This approach leads to a limitation on our time step, but significant time saving, approximately an order of magnitude, is gained due to the use of FFT for the Poisson system.

The simulations were run with constant time step, and the CFL number is variable but restricted below 0.2,

$$\frac{\Delta t}{\mathrm{CFL}} = \min\left\{ \left(\frac{|u|}{2\Delta x} + \frac{|v|}{2\Delta y} + \frac{|w|}{2\Delta z} + \frac{4}{Re}\left(\frac{1}{\Delta x^2} + \frac{1}{\Delta z^2}\right)\right)^{-1}, \sqrt{\frac{\rho \Delta x^3}{\sigma}}, \sqrt{\frac{\rho \Delta x}{k_s}} \right\}. \tag{3.3}$$

The first requirement is the usual restriction for the stability of the time integration of the viscous and convective terms, while the other two are restrictions for the deformation of the gas–liquid interfaces and solid–liquid interfaces. All deformable interface simulations take the initial fields from flow snapshots of flat interface simulations (Seo *et al.* 2015). When the interface is allowed to deform, there is an initial transient period for the interface to evolve to a statistically steady state. The simulations were run for at least $20\delta/u_\tau$ after the initial snapshot, where δ/u_τ is the characteristic turnover time for the largest turbulent eddies. The first $3\delta/u_\tau$ interval was left out of the statistical sampling, to avoid contamination by initial transients from the simulation with flat interfaces.

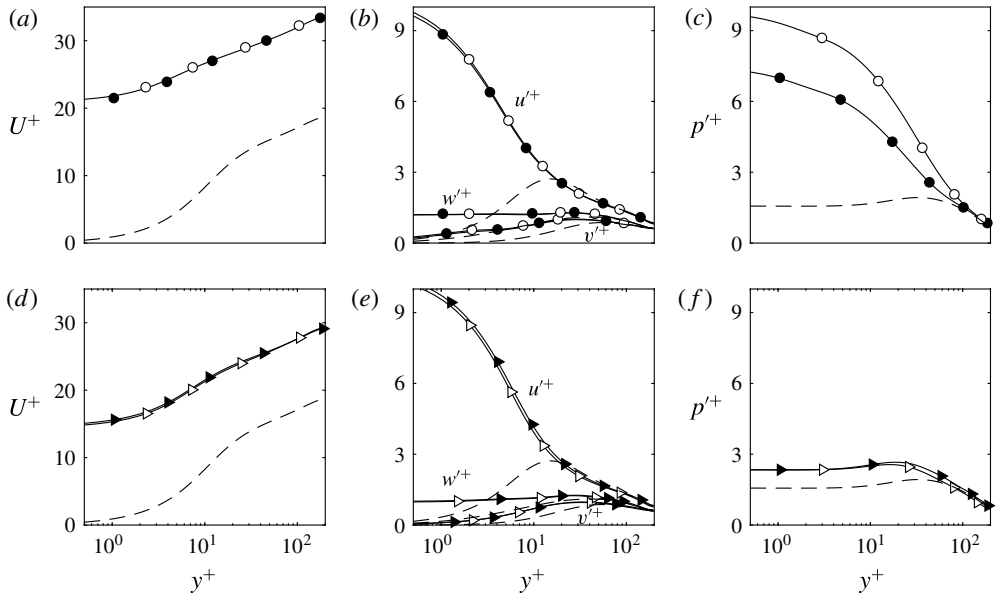

FIGURE 4. Comparison of statistics at $L^+ \approx 155$, $w^+ \approx 52$ at $Re_\tau \approx 200$. (*a*,*d*) Mean streamwise velocity profile; (*b*,*e*) three components of velocity root-mean-square (r.m.s.) fluctuations; (*c*,*f*) pressure r.m.s. fluctuations. –●–: P155, posts with $We_L = 0$ (Seo *et al.* 2015); –○–: P155W2, posts with $We_L = 2 \times 10^{-3}$; –▷–: R155, streamwise ridges with $We_L = 0$ (Seo *et al.* 2015); –▶–: R155W2, streamwise ridges with $We_L = 2 \times 10^{-3}$; – – – –: smooth walls, $Re_\tau \approx 200$ (Seo *et al.* 2015).

4. DNS results

4.1. *Effects of interface deformation*

4.1.1. *Turbulence statistics*

First, we investigate the impact of the deformability of the gas–liquid interface on turbulence statistics. Figure 4 presents a comparison of flow statistics between simulations with flat gas–liquid interfaces ($We^+ = 0$) and those with deformable interfaces. It is apparent that the kinematic statistics, including mean flow and root-mean-square (r.m.s.) of velocity fluctuations, are not affected by the interface deformability, while pressure fluctuations are significantly affected in the cases in which the surface texture consisted of isotropic posts. The drag reduction is thus unchanged by deformability of interface, as shown in table 1. The fact that the mean flow is not affected by the interface deformability implies that the slip velocity can be estimated from the relations proposed by Seo & Mani (2016). Using DNS of flows over flat but patterned interfaces, Seo & Mani (2016) identified two scaling regimes for the slip velocity U_s^+, which is also equal to the slip length, b^+, when reported in wall units. For small textures they found $U_s^+ \sim L^+/\sqrt{\phi_s}$, while for large textures $U_s^+ \sim L^{+(1/3)}/\sqrt{\phi_s}$. We will later use these relations to approximate We_s.

Figure 4 indicates that, even in cases with a flat interface, there is a significant difference between pressure fluctuations in post versus ridge geometry. This difference is shown to be due to stagnation pressure induced by slipping flow in the streamwise direction that encounters the leading edge of solid posts (Seo *et al.* 2015). However, here we show that interface deformability further increases the near-wall pressure

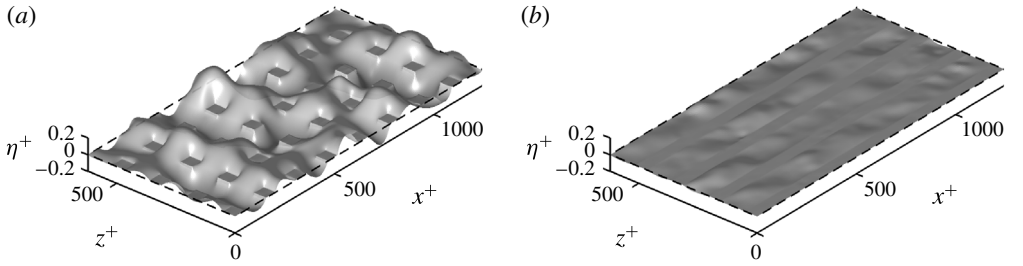

FIGURE 5. Comparison of instantaneous interface heights, $\eta^+ = \eta/\delta_v$, for two different superhydrophobic textures for $Re_\tau \approx 200$, $L^+ \approx 155$ and $We_L = 2 \times 10^{-3}$. (*a*) Posts, P155W2, (*b*) streamwise ridges, R155W2. The dashed lines are the baseline wall location $y^+ = 0$. The axis for η^+ is 300 times magnified for visualization purposes.

fluctuations. This increase is significant in the case of surfaces with distributed posts, which are better representative of realistic scenarios where superhydrophobic surfaces are manufactured by sprayed coatings and/or etching processes compared to streamwise ridges.

4.1.2. *Interface deformations*

We show deformations of gas–liquid interfaces in viscous units η^+, for the isotropic posts and the streamwise ridges with $L^+ \approx 155$ and $We_L = 2 \times 10^{-3}$ in figure 5. For the isotropic posts, the time-averaged statistics of the maximum magnitude of interface deformation is $\overline{|\eta|^+_{max}} = 0.30$ and the r.m.s. of the interface fluctuation (in time and space) is $\eta^+_{rms} = 0.09$. For the streamwise ridges, the interface deformation is much smaller than the isotropic posts, $\overline{|\eta|^+_{max}} = 0.06$, $\eta^+_{rms} = 0.01$. The maximum η^+ and minimum η^+ is 0.9 and -0.9 in wall units and the maximum of the interface angle in the streamwise direction is 1.8° for the case of $L^+ = 155$ and $We_L = 4 \times 10^{-3}$. All of these interface fluctuations are very small compared to either channel height or viscous lengths; therefore, the effect of surface deformation does not alter the mean and fluctuations of velocity profiles in turbulent statistics.

4.1.3. *Pressure fluctuations on gas–liquid interfaces*

To better understand the augmented pressure fluctuations near the wall, we plot instantaneous wall pressure snapshots with flat and deformable interfaces in figure 6. A comparison of wall pressure fluctuations (figure 6) with a corresponding interface deformation (figure 5) shows that positive pressure loads deflect the interface downwards and negative pressure loads deflect it upwards.

The pressure fluctuations on deformable interface on isotropic posts have distinct spanwise-coherent structures, which can be seen best in figures 6(*b*) and 7. The stagnation pressure induced by slipping flows, as in the case with a flat interface (Seo *et al.* 2015), still remains on the deformable interface and the spanwise-coherent pressure appears superposed on top of the stagnation pressure. The phase-shift relation between wall deformation and pressure, and spanwise-coherent pressure waves have been observed for turbulent flows over compliant walls, in which the wall is responding to the overlying pressure fluctuations (Kim & Choi 2014), although in that case the compliant wall has zero tangential velocity. Streamwise ridges have no notable changes on wall pressure fluctuations. Therefore, in the remaining portion of the paper, we focus on the analysis of flow interactions with post textures.

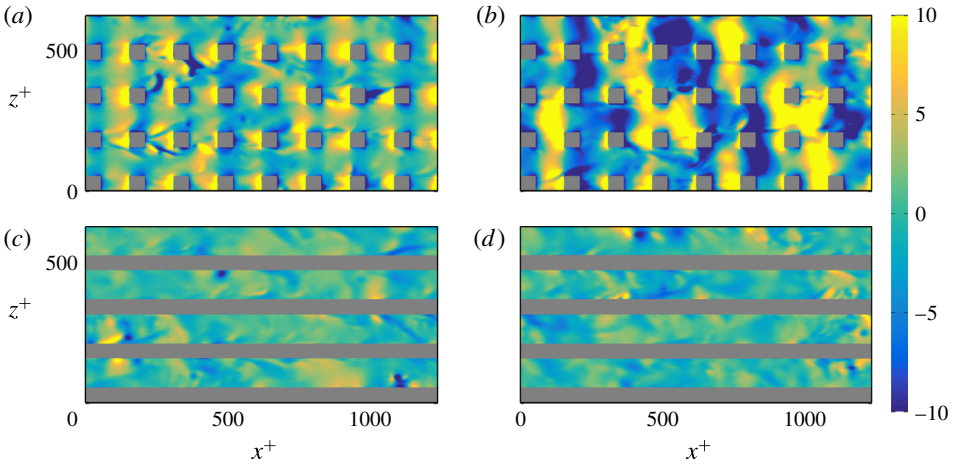

FIGURE 6. (Colour online) Comparison of instantaneous pressure contours, $p^+ = p/(\rho u_\tau^2)$, at $y^+ = 0$, for cases at $Re_\tau \approx 200$, and $L^+ \approx 155$. (*a*) P155, $We_L = 0$, (Seo *et al.* 2015) (*b*) P155W2, $We_L = 2 \times 10^{-3}$, (*c*) R155, $We_L = 0$, (Seo *et al.* 2015) (*d*) R155W2, $We_L = 2 \times 10^{-3}$. From blue to yellow, the fluctuations range between -10 and 10 wall units. Snapshots from cases with finite surface tension are taken at the same instance in which the interface deformations in figure 5 are taken. The main flow direction is left to right.

Compared to streamwise ridges, post structures better represent practically scalable superhydrophobic surfaces, such as those manufactured by sprayed coatings.

4.1.4. *Space–time characteristics of the pressure wave*

A remarkable feature of the detected spanwise-coherent pressure, which we will refer to as flow-induced capillary waves, is upstream propagation. Successive time snapshots of the pressure fluctuations on deformable interfaces are portrayed in figure 7 (supplementary movies are available on https://doi.org/10.1017/jfm.2017.733). In figure 7, the spanwise-coherent pressure travels upstream, with a rough wavelength in the streamwise direction $\lambda_x^+ \approx 2L^+$. While the pressure patches sporadically break and reform as time progresses, they sustain coherent structures indicated by the same sign of pressure bands across the spanwise direction. In figure 7, the time period for a coherent structure is $T \approx 10\delta_v/u_\tau$. This propagation of spanwise-coherent pressure is clearly different from the Kelvin–Helmholtz-type wave due to its direction against the main flow.

Quantitative representations of the upstream-travelling wave are obtained through space–time correlations of the wall pressure signal plotted in figure 8. To obtain space–time correlations for only 'dynamic' components of the pressure fluctuations, excluding stagnation pressure, we subtract the mean stationary pressure from the instantaneous pressure data. In figure 8(*a*), the correlation for the deformable interface case distinctively shows two separate motions at the interface, one aligned with the flow direction ($U_{c_1}^+ > 0$), and another opposed to the flow direction ($U_{c_2}^+ < 0$). This is in contrast to the space–time correlation of pressure from the simulation with a flat interface in figure 8(*b*), which has unidirectional convection in the direction of the mean flow. The first velocity component, $U_{c_1}^+ \approx 24$, is the advection of near-wall turbulence, which is equivalent to the value from the simulation with a flat interface. Due to slippage on the wall, $U_s^+ = 21$, this convection velocity is larger than

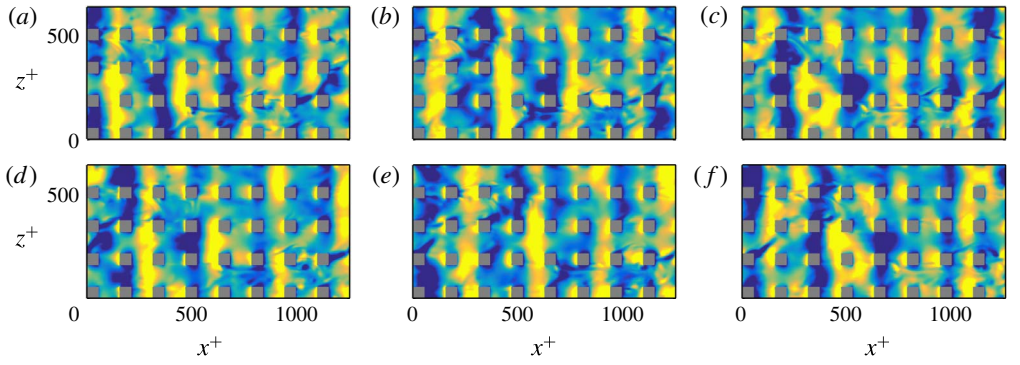

FIGURE 7. (Colour online) Successive instantaneous snapshots of wall pressure fluctuations, p^+, in time for P155W2 with $Re_\tau \approx 200$, $L^+ \approx 155$ and $We_L = 2 \times 10^{-3}$. From (*a*) to (*f*), $t = t_0 + [0:2:10]\ \Delta t$, where $\Delta t = \delta_v/u_\tau$. The main flow direction is left to right. From blue to yellow, the fluctuations range between -10 and 10 wall units.

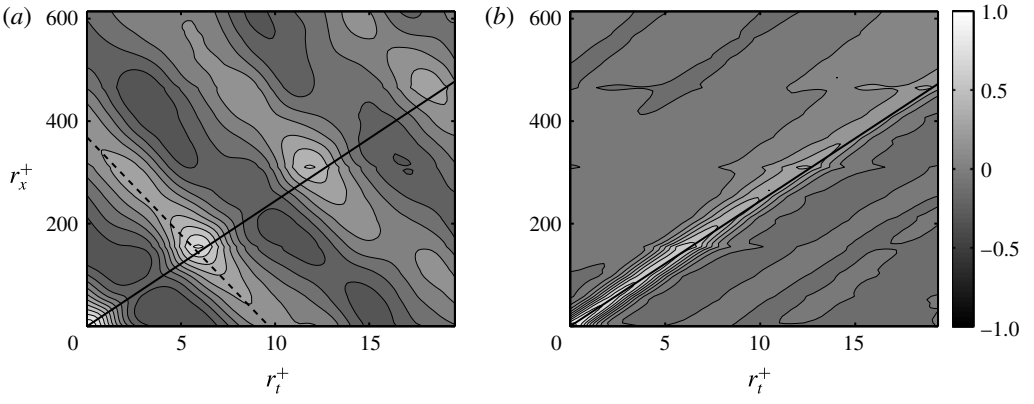

FIGURE 8. Comparison of space–time correlations of dynamic pressure signals, p^+ at $y^+ = 0$, for cases with $Re_\tau \approx 200$ and $L^+ \approx 155$. From black to white, the correlation ranges between -1 and 1. (*a*) $We_L = 2 \times 10^{-3}$, (*b*) $We_L = 0$. The solid lines represent the mean advection of the turbulent eddies, $U_{c_1}^+ \approx 24$. The dashed line represents the phase velocity of the upstream-travelling, spanwise-coherent structures, $U_{c_2}^+ \approx -38$.

the advection of turbulence pressure produced by traditional smooth no-slip walls, $U_c^+ \approx 13$ (Kim 1988; Choi & Moin 1990; Kim & Hussain 1993). On the other hand, the upstream-travelling pressure is solely an outcome of the interface deformability. For the considered case, the spanwise-coherent upstream-travelling waves have a convection velocity of $U_{c_2}^+ \approx -38$. The wavelength in the streamwise direction is approximately twice the texture wavelength, $\lambda_x \approx 380\delta_v$, and the time period is $T \approx 10\delta_v/u_\tau$. λ_x and T can be quantified from the intercept of the correlation ridge (dashed line) with the axis in figure 8(*a*).

4.2. *Reynolds number dependence*

Next, we examine the dependence of the upstream-travelling capillary waves on system parameters in wall units. We first change the friction Reynolds number from

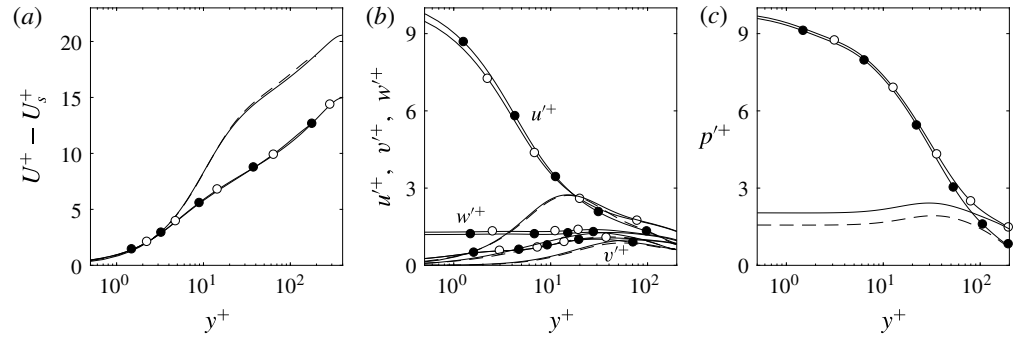

FIGURE 9. Comparison of statistics for posts geometries with $L^+ \approx 155$, $We_L = 2 \times 10^{-3}$ at $Re_\tau \approx 200$ and $Re_\tau \approx 400$. (*a*) Mean streamwise velocity profile minus the slip velocity; (*b*) velocity r.m.s. fluctuations; (*c*) pressure r.m.s. fluctuations. –●–, P155W2, posts at $Re_\tau \approx 200$; – – – –, smooth walls, $Re_\tau \approx 200$; –○–, P155W2$_{Re}$, posts at $Re_\tau \approx 400$; ——, smooth walls, $Re_\tau \approx 400$.

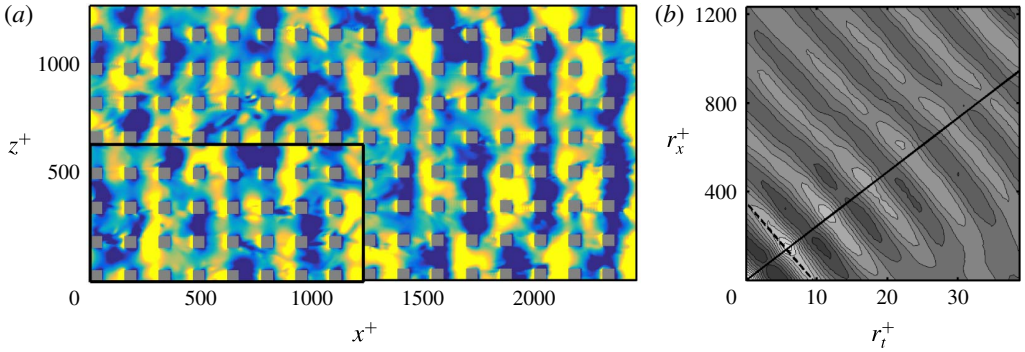

FIGURE 10. (Colour online) (*a*) Instantaneous pressure contours, p^+, at $y^+ = 0$ for the P155W2$_{Re}$ case with $L^+ \approx 155$, $We_L = 2 \times 10^{-3}$ at $Re_\tau \approx 400$. Inset figure in the bottom left quarter of figure is an overlay of instantaneous pressure contours at $Re_\tau \approx 200$. From blue to yellow, the fluctuations range between -10 and 10 wall units. (*b*) Space–time correlations of dynamic pressure signals at $Re_\tau \approx 400$. ——: $U_{c_1}^+ \approx 24$; – – – –: $U_{c_2}^+ \approx -38$. From black to white, the correlation ranges between -1 and 1.

$Re_\tau \approx 200$ to $Re_\tau \approx 400$ and investigate the effect of Re_τ. In figure 9, turbulence statistics show that the near-wall behaviour of superhydrophobic surfaces with a deformable interface is essentially independent of Reynolds number when the other parameters are fixed in wall units. The mean quantities at the wall, for instance the slip velocity or the wall pressure, are well collapsed to the same values at two Reynolds numbers. The statistics away from the wall are identical to the outer region of smooth-wall channel flows and consistent with previous studies. The investigation of wall pressure in figure 10(*a*) qualitatively confirms that the structure of the flow-induced capillary waves remains essentially unmodified. Space–time correlation of the pressure signal in figure 10(*b*) further confirms that the convection velocity of higher Reynolds number, $U_{c_2}^+ \approx -38$, is unaltered from the lower Reynolds number simulation. Therefore, we believe our current results near the gas–liquid interface

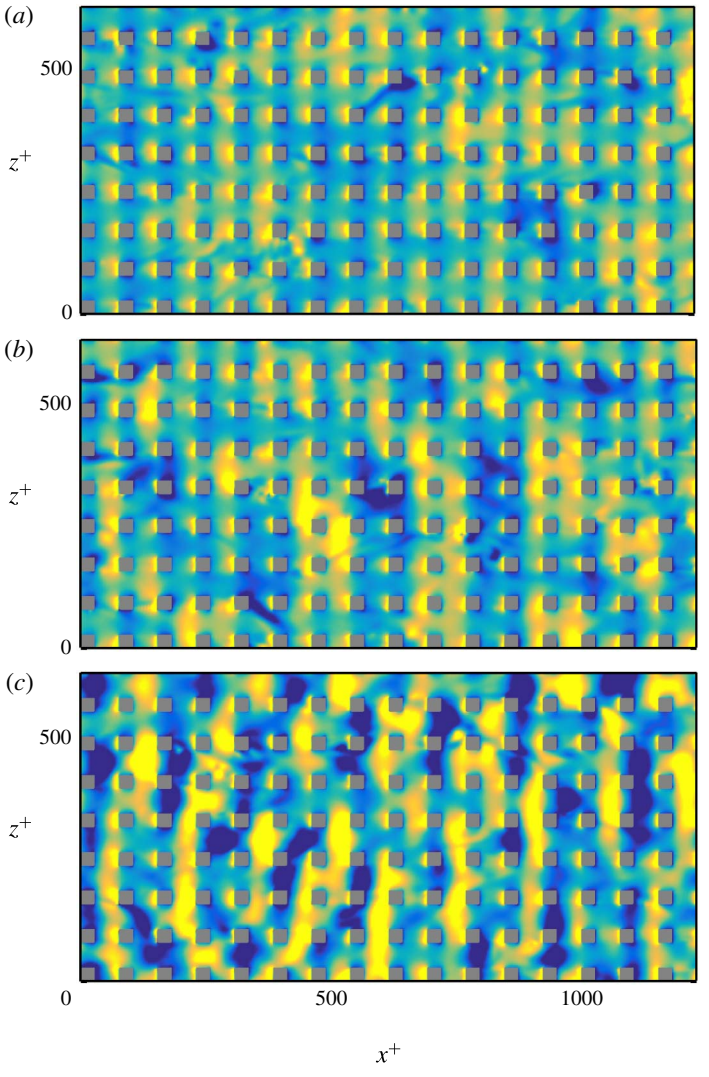

FIGURE 11. (Colour online) Instantaneous wall pressure, p^+, contours for cases with $Re_\tau \approx 200$ and $L^+ \approx 77$. (*a*) $We_L = 10^{-3}$, (*b*) $We_L = 2 \times 10^{-3}$, (*c*) $We_L = 4 \times 10^{-3}$.

can be extended to higher Reynolds numbers, and the characteristics of pressure fluctuations are mainly governed by L^+ and We_L.

4.3. *Effect of surface tension*

In DNS, we systematically change We_L and investigate how the dynamic characteristics of pressure changes. In figure 11, we plot instantaneous realizations of wall pressure with three different Weber numbers for $L^+ \approx 77$. As We_L increases, the spanwise-coherent pressure becomes dominant and its magnitude intensifies. In addition, it is visually shown that the wavelength λ_x^+ changes with We_L. For instance, wavelength becomes shortened approximately from $\lambda_x^+ \approx 3L^+$ to $\lambda_x^+ \approx 2L^+$ as We_L increases from 2×10^{-3} to 4×10^{-3}.

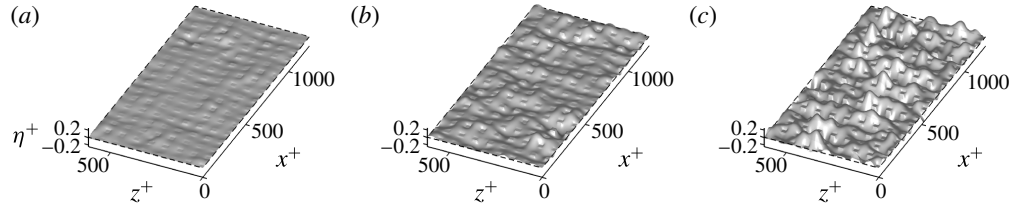

FIGURE 12. Instantaneous interface deformation, η^+, for cases with $Re_\tau \approx 200$ and $L^+ \approx 77$. (*a*) $We_L = 10^{-3}$, (*b*) $We_L = 2 \times 10^{-3}$, (*c*) $We_L = 4 \times 10^{-3}$. The dashed lines represent the baseline wall location $y^+ = 0$. Snapshots are taken at the same instance in which the pressure snapshots in figure 11 are taken. The dashed lines are the baseline wall location $y^+ = 0$. The axis for η^+ is 300 times magnified for visualization purposes.

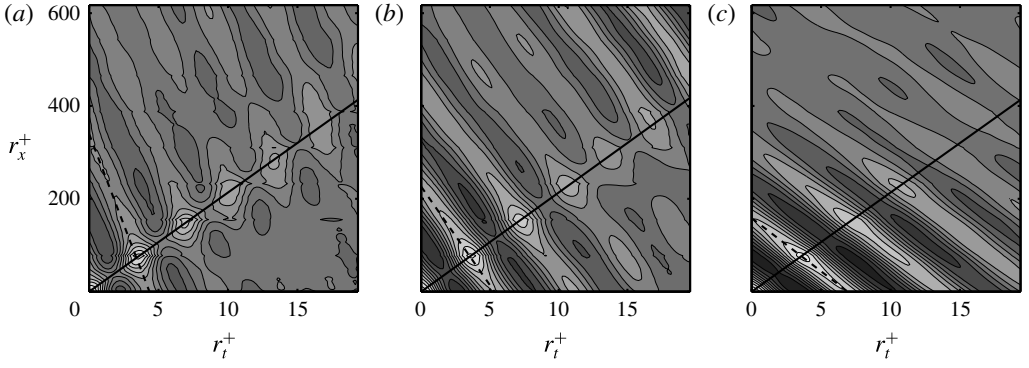

FIGURE 13. Comparison of space–time correlations of dynamic wall pressure signals, p^+, for cases with $Re_\tau \approx 200$ and $L^+ \approx 77$. (*a*) $We_L = 10^{-3}$, – – –: $U_{c_2}^+ \approx -23$; (*b*) $We_L = 2 \times 10^{-3}$, – – –: $U_{c_2}^+ \approx -42$; (*c*) $We_L = 4 \times 10^{-3}$, – – –: $U_{c_2}^+ \approx -78$. ——: $U_{c_1}^+ \approx 21$ for all cases.

The consequent interface fluctuations in figure 12 intensify with larger We_L in response to the increased spanwise-coherent pressure. The large deformation of the interface implies that the gas–liquid interface becomes less stable when We_L increases.

In figure 13, the space–time correlations of the pressure signal show that for the larger We_L, λ_x^+ becomes shorter, the wave period, T^+ becomes longer, and thus U_c^+ becomes slower. The advection of turbulence remains unchanged,$U_{c_1}^+ \approx 21$, regardless of the change of We_L since slip velocity is the same for same L^+. That is, the advection of turbulence is not affected by pressure fluctuations imposed by deformability of the interface while the upstream-travelling wave is strongly dependent on the Weber number.

4.4. *Dependence on the texture size*

Next, we investigate the effect of texture size by reducing the texture size down to $L^+ \approx 13$. In figure 14, we portray wall pressure snapshots with texture size spanning $L^+ \approx 26$–77 at fixed $We_L = 4 \times 10^{-3}$ and $Re_\tau \approx 200$. At texture size $L^+ \approx 26$, the stagnation pressure and the footprint from overlying turbulence, which scales $\sim 100\delta_v$, are dominant components of the total pressure fluctuations, and the pressure due to the capillary wave is hard to recognize. The weakness of the

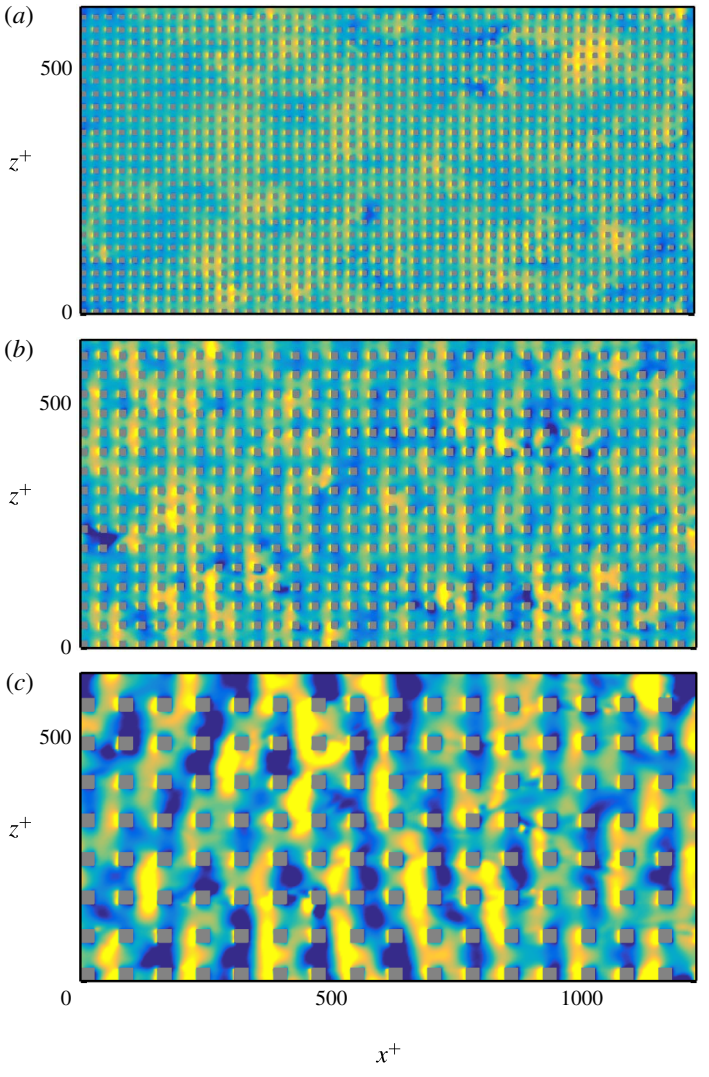

FIGURE 14. (Colour online) Instantaneous wall pressure contours, p^+ with (*a*) $L^+ \approx 26$, (*b*) $L^+ \approx 38$, (*c*) $L^+ \approx 77$ at $We_L = 4 \times 10^{-3}$ and $Re_\tau \approx 200$. From blue to yellow, the fluctuations range between -10 and 10 wall units.

capillary pressure holds for smaller texture size $L^+ \approx 13$, and in that case the capillary pressure is completely overwhelmed by other fluctuations so that only the downstream-propagating component remains in the space–time correlation analysis. These results indicate that the deleterious effect of spanwise-coherent waves on the stability of gas pockets becomes significant when L^+ becomes large.

The phase velocity, wavelength, and time scale of the capillary wave covering a wide range of L^+ and We_L are summarized in figure 15. The wavelength and time period are calculated from space–time correlations of the capillary pressure. The averaged data from at least four different uncorrelated time windows are plotted with error bars. The results show that λ_x^+ is comparable to several times L^+, and becomes longer for increasing L^+ under the same We_L. With larger L^+ for fixed We_L, the time

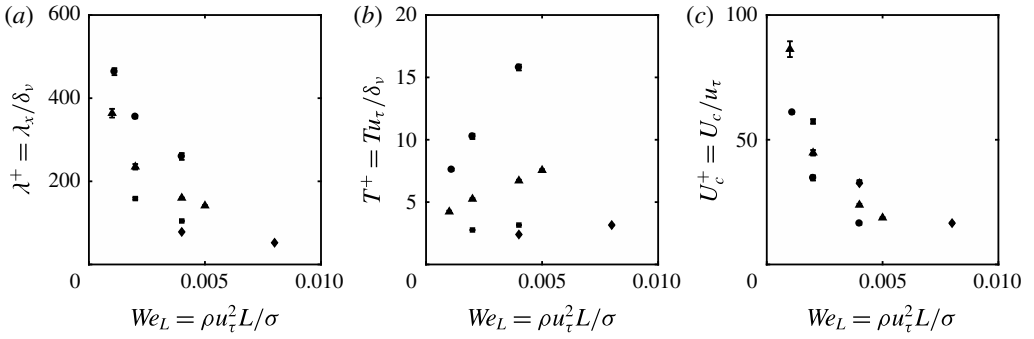

FIGURE 15. Statistics of interfacial quantities scaled in viscous units versus We_L. (*a*) Wavelength of upstream-travelling wave in the streamwise direction, λ_x^+; (*b*) time period of the upstream-travelling wave, T^+; (*c*) convection velocity of the upstream-travelling wave, U_c^+. ◆: $L^+ \approx 26$, ■: $L^+ \approx 38$, ▲: $L^+ \approx 77$, ●: $L^+ \approx 155$. Symbols are computed by averaging at least four uncorrelated signals, and error bars plotted on top of the symbols.

scale of the capillary waves increases, and the convection speed decreases. In the present form, the data do not show collapse on any of the measured quantities.

4.5. *Data collapse with We_s*

So far we have reported the capillary wave speed, wavelength, and period in wall units, i.e. u_τ, δ_v, for length and velocity scales. The friction Reynolds number independence shown in § 4.2 indicates that the interfacial phenomena would be not directly connected to the overlying outer turbulence scales. Since the interface deformation is small and its effect is confined to the near-wall region, we hypothesize that the interfacial phenomena are separable from the scales associated with the overlying turbulence. In this case, a more suitable set of reference dimensions would be the texture size, L, and the flow slip velocity, U_s.

In figure 16, we rescale the wavelength, time frequency, and convection velocity with L and U_s. As a result, the dimensionless time $T^* = TU_s/L$ and velocity $U_c^* = U_c/U_s$ show excellent collapse when scaled with $We_s = \rho U_s^2 L/\sigma$. The dimensionless wavelength $\lambda^* = \lambda_x/L$ shows reasonable collapse. This data collapse reveals that the main parameter governing the interfacial flow is We_s. This result supports the hypothesis that the observed coherent pressure waves are capillary waves that develop as modes of oscillation of the interface as a membrane.

5. A semianalytical model for the induced capillary waves

In this section we study the dynamics of interfacial waves by a simple analytical model to better understand the observed phenomena from DNS. We have developed a simplified model for prediction of natural frequency modes associated with flexible, free slip interfaces in between solid posts.

5.1. *Model formulation*

We consider an inviscid flow of density ρ slipping over a superhydrophobic surface with posts separated by a distance L, with uniform mean velocity U, and with small

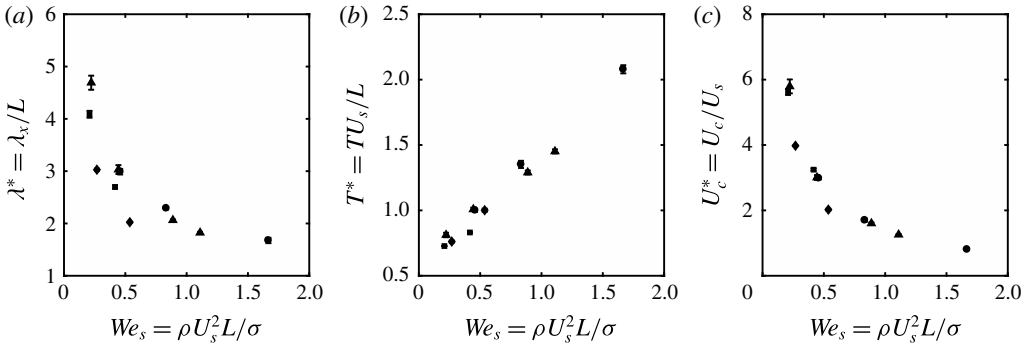

FIGURE 16. Statistics of interfacial quantities scaled with L and U_s versus We_s. (*a*) wavelength of the upstream-travelling wave scaled by the texture size, $\lambda^* = \lambda_x/L$; (*b*) time frequency of the upstream-travelling wave, $T^* = TU_s/L$; (*c*) convection velocity of the upstream-travelling wave scaled by the slip velocity, $U_c^* = U_c/U_s$. ◆: $L^+ \approx 26$, ■: $L^+ \approx 38$, ▲: $L^+ \approx 77$, ●: $L^+ \approx 155$.

fluctuations (u, v, w; p) on the mean flow induced by a deformable interface with finite surface tension σ. This problem is analogous to the wave propagation in liquid films (Squire 1953; Taylor 1959), except for the presence of the solid posts, which make the film discontinuous. The base state involves a uniform streamwise velocity, with no interface deformation, which trivially satisfies the Euler equation, continuity, and the no-penetration condition on the interface. The fluctuating velocity field can be described in terms of a potential $\psi(x, y, z)$, which satisfies

$$\nabla^2 \psi = 0. \tag{5.1}$$

Using Fourier decomposition along the wall-parallel directions (x and z), the above Poisson equation adopts the form $(-k_x^2 - k_z^2 + \partial_y^2)\,\widehat{\psi} = 0$ for each (k_x, k_z) mode, where $\widehat{\psi}$ means Fourier coefficient of ψ. For vanishing $\widehat{\psi}$ at $y \to \infty$, the solution is $\widehat{\psi}(y) = \widehat{\psi}_{y=0} \exp(-\sqrt{k_x^2 + k_z^2}\, y)$. This allows us to establish a relationship at $y = 0$ between the potential and its y-derivative,

$$(\partial_y \psi)_{y=0} = \boldsymbol{F}^{-1} \boldsymbol{K} \boldsymbol{F} \psi_{y=0}, \tag{5.2}$$

where $\boldsymbol{F}$ and $\boldsymbol{F}^{-1}$ denote discrete direct and inverse discrete Fourier transform operators, and $\boldsymbol{K}$ is the diagonal matrix formed by the derivative eigenvalues $-\sqrt{k_x^2 + k_z^2}$. Note that, by the definition of the potential, $\partial_y \psi = v$. Therefore, we are interested only in the restriction of (5.2) that also satisfies $(\partial_y \psi)_{y=0} = v_{y=0} = 0$ over the solid posts.

The potential ψ can also be related to the fluctuating pressure through the linearized inviscid momentum equation,

$$(\partial_t + U\partial_x)\psi = -\frac{1}{\rho} p, \tag{5.3}$$

which can be particularized at $y = 0$. Let us also note that the fluctuating deformation of the interface satisfies the Young–Laplace equation

$$(\partial_x^2 + \partial_z^2)\eta = \frac{1}{\sigma} p, \tag{5.4}$$

where η is connected to the wall-normal velocity through the material derivative,

$$(\partial_t + U\partial_x)\eta = (\partial_y \psi)_{y=0}. \tag{5.5}$$

We are interested in wave solutions of the fully coupled system of equations (5.2)–(5.5). Using the corresponding transformation $\partial_t = \mathrm{i}\omega$, the problem can be written in the frequency-ω domain,

$$\boldsymbol{A}(\omega)\psi_{y=0} = 0, \tag{5.6}$$

where the dependence of $\boldsymbol{A}$ on ω is quadratic. The problem then reduces to finding values of ω for which the determinant of $\boldsymbol{A}$ is zero, and the corresponding eigen-solutions in the null subspace. The above system of equations can be normalized using reference scales of length, $L_r = L$, velocity $U_r = U$, which lead to subsequent scales of time, $T_r = L/U$, pressure, $p_r = \rho U^2$, and surface tension $\sigma_r = \rho U^2 L$. In the end, the dimensionless system of equation requires only one physical input parameter – that is, the Weber number, $We = \rho U^2 L/\sigma$. Solutions exist only for a discrete set of frequencies $\omega^* = \omega L/U$, and take the form of either upstream- or downstream-travelling waves with a phase velocity U_c that can be several times larger than the flow velocity U.

5.2. *Methodology*

To solve problem (5.6) numerically, we have used a second-order, central finite-difference scheme on a uniform grid to discretize equations (5.3)–(5.5), with $\Delta x = L/24$ and $\Delta z = L/24$. The domain is a periodic box in x and z. The domain size is an integer number of L.

This semianalytical approach is used to predict the natural frequency of capillary waves observed in DNS. The first solution for ω^* spans the full domain considered, thus the wavelength associated with the first frequency mode must be determined *a priori* for the model prediction. We provide the analytical model with wavelengths from several cases observed from DNS, mostly close to an integer number of L. To establish a corresponding U, the most reasonable choice is to use U_s^+ from those DNS cases. In that case, note that We is actually the Weber number based on slip velocity, $We_s = \rho U_s^2 L/\sigma$.

5.3. *Results*

We find that the first solution, that of smallest ω^*, is always an upstream-travelling, spanwise-coherent wave. A solution corresponding to the DNS case $P155W2$ when using U_s^+ to estimate We_s is portrayed as an example in figure 17. The qualitative structure and behaviour of travelling pressure is similar to the DNS case, though the DNS case shows more complex behaviour. In DNS, the random nature of overlying turbulence changes the pressure fluctuations in time and space as opposed to simple periodic analytical solutions. DNS is also likely to contain multiple modes of capillary waves while only the most dominant mode is detected in the space–time correlation analysis. However, an explanation of the mechanism energizing these modes has yet to be provided.

To capture the solutions observed in our DNS with $\lambda_x \approx 2L - 4L$ over a wide range of L^+ and We_L, we seek solutions for (5.6) in a domain of length λ_x. The values of the dimensionless $We_s = \rho U_s^2 L/\sigma$ for the model are chosen to match our DNS set-ups. Table 2 compiles solutions for We_s values estimated using U_s^+, and for values of λ_x/L

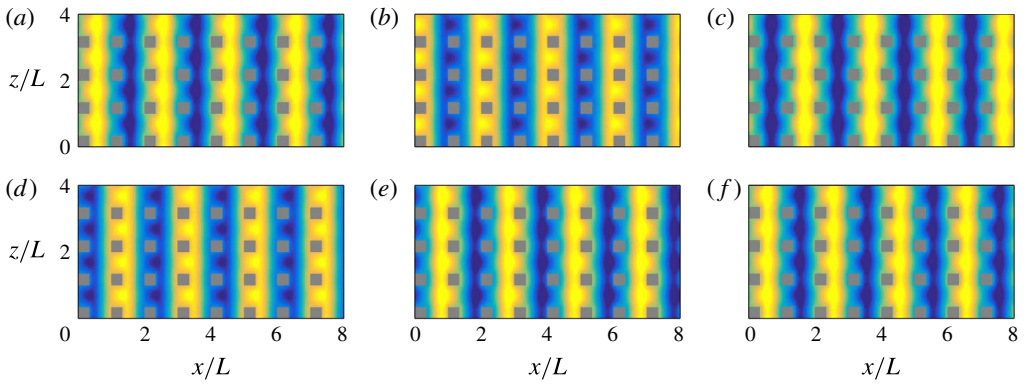

FIGURE 17. (Colour online) Successive instantaneous realizations of the pressure at $y=0$ for the model problem with $\lambda_x=2L$ and $\omega\approx 6.1U/L$. From (a) to (f), $t=t_0+2\pi/\omega\times[0:0.2:1]$.

DNS	U_s^+	We_s	$(\lambda_x/L)_{DNS}$	$\lambda^*{}_{model}$	ω^*_{model}	$U^+_{c,model}$	$U^+_{c2,DNS}$
P78W4	14.9	0.888	2.1	2	5.8	27.3	24.2
P155W2	20.4	0.833	2.3	2	6.1	39.3	34.7
P78W2	14.9	0.444	3.2	3	7.1	50.5	46.4
P155W1	20.4	0.417	3.0	3	7.4	72.2	61.0
P39W2	10.2	0.208	4.1	4	9.5	62.0	57.3

TABLE 2. Solutions to the linearized, inviscid flow over superhydrophobic posts. From each DNS, U for the model is estimated as the slip velocity, $U=U_s$ to obtain a Weber number $We_s=We_L U_s^{+2}$. From all the possible frequencies $\omega^*=\omega L/U$ for which (5.6) is satisfied, only the one with wavelength $\lambda^*=\lambda_x/L$ close to that observed in the DNS is shown. U_c^+ is the convection velocity of the corresponding solution, for which the model $U^+_{c,model}$ is to be compared with that measured from the DNS, $U^+_{c,DNS}$.

close to those observed in the DNS. The results of convective speed, U_c^+, predicted by the semianalytical model agree reasonably well with those measured from space–time correlation of the DNS data. The model can predict not only the direction of propagation of these modes, but also the magnitude of the propagation velocity versus We_s.

5.4. *A dispersion relation of semianalytical capillary waves*

In order to develop some intuition about the prediction of the semianalytical model, in this section we present a comparison between the results of this model and phenomenological scaling laws of the frequency versus wavelength relations. We note, however, this comparison is made in simplifying limits and regimes that do not necessarily represent the considered turbulent flow scenarios. We first recall that in the small-capillary-wavelength limit, $\lambda^*=\lambda/L\ll 1$, the texture would not affect the capillary waves, and the standard theory would be capable of predicting the dispersion relation.

This scaling can be obtained by combining a system of equations from (5.3) to (5.5), providing $\omega\psi\sim P/\rho$, $\eta/\lambda^2\sim P/\sigma$, and $\omega\eta\sim\psi/\lambda$, therefore $\omega\sim\sqrt{\sigma/(\rho\lambda^3)}$.

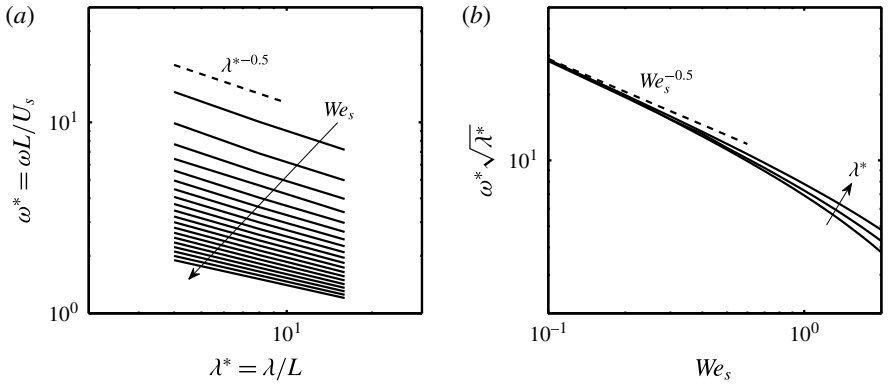

FIGURE 18. Dimensionless time frequency solutions, ω^*, from the semianalytical model. (*a*) ω^* versus λ^* with an arrow with increasing $We_s = 0.1$–2.0 with successive interval 0.1. (*b*) $\omega^*\sqrt{\lambda^*}$ versus We_s with an arrow with increasing $\lambda^* = 2^2, 2^3, 2^4$.

When scaled with L and U_s, the time frequency associated with this wave, $\omega^* \equiv \omega L/U_s$, would be

$$\omega^* \sim We_s^{-0.5}\lambda^{*-1.5}. \tag{5.7}$$

In the large-wavelength-limit $\lambda \gg L$, however, this scaling should be modified. When the wavelength is sufficiently larger than texture size, one can assume that dependence of pressure on the amplitude would scale as $p \sim \sigma\eta/L^2$. This is because the dominant spatial variation of the capillary wave would depend on L. This relation combined with $\omega\psi \sim P/\rho$, and $\omega\eta \sim \psi/\lambda$, results in $\omega \sim \sqrt{\sigma/(\rho\lambda L^2)}$. The consequent dimensionless frequency of the wave is

$$\omega^* \sim We_s^{-0.5}\lambda^{*-0.5}. \tag{5.8}$$

In this analysis, in addition to the large-wavelength limit, we also assume that the capillary speed, $U_c \sim \sqrt{\sigma\lambda/(\rho L^2)}$, is much larger than the slip velocity, U_s, and thus the effect of the background advection can be ignored (i.e., small We_s). In figure 18, we show log–log plots of time frequency of the interface from a semianalytical solution for the range of $0.1 \leqslant We_s \leqslant 2.0$ and $2^2 \leqslant \lambda/L \leqslant 2^4$. In figure 18(*a*), the semianalytical model shows the expected inverse square root scaling for λ^* for the whole range of We_s. In figure 18(*b*), the frequency is rescaled with $w^*\sqrt{\lambda^*}$. As λ^* becomes large, $\lambda^* \gg 1$, the whole range of We_s exhibits the inverse square root scaling with respect to We_s, as expected from (5.8).

While this phenomenological scaling provides an understanding of the dispersion relations in the induced capillary waves, the DNS data does not necessarily fall in the assumed simplified regimes considered here. Therefore, the prediction of dispersion relations in the DNS results requires comparison with the full semianalytical model. Another shortcoming is that the provided scalings do not predict which capillary wavelength(s) are most energized by the overlying turbulent flow, neither do they predict the amplitude of these waves in the statistically stationary condition. In the next section we use DNS data directly to infer scaling laws predicting the capillary wavelength and amplitude in terms of input conditions. In the discussion section we suggest possible methods for a physics-based explanation of these observations.

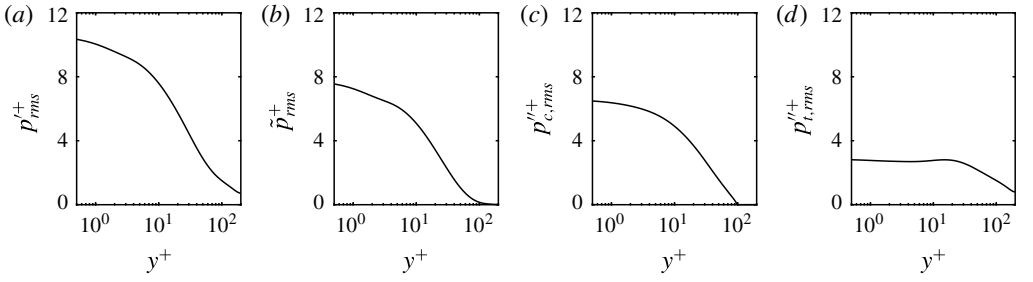

FIGURE 19. Decomposition of wall pressure fluctuations for $L^+ \approx 155$ and $We_L = 4 \times 10^{-3}$. (*a*) total r.m.s. pressure fluctuation, p'^{+}_{rms}, (*b*) r.m.s. stagnation pressure fluctuation, $\tilde{p}^{+}_{rms}$, (*c*) r.m.s. capillary pressure $p''^{+}_{c,rms}$, (*d*) r.m.s. turbulence pressure, $p''^{+}_{t,rms}$.

6. On the scaling of capillary pressure and interface deformation

6.1. *Amplitude of capillary pressure and interface deformation*

To assess the magnitude of flow-induced capillary pressure fluctuations, we decompose the spatio-temporal pressure fields. We have identified three separate phenomena contributing to pressure fluctuations: the overlaying turbulent flow, stagnation phenomena, and capillary waves. First, we exclude the effect of stagnation pressure by a decomposition of the total signal to obtain an unsteady signal, p'', so that

$$p''(x, z, y, t) = p(x, z, y, t) - \bar{p}(y) - \tilde{p}(\tilde{x}, \tilde{z}, y), \tag{6.1}$$

where $\bar{p}(y)$ is averaged pressure over wall-parallel domain and time, and $\tilde{x} = \text{modulo}(x, L_x)$ and $\tilde{z} = \text{modulo}(z, L_z)$ are the periodic streamwise and spanwise coordinates within each pattern unit. The stagnation component $\tilde{p}$ is averaged over time and over the number of periodic units. The above decomposition method, first introduced by Reynolds & Hussain (1972), was used to analyse turbulent flows over stagnation wall modifications (Choi, Moin & Kim 1993; García-Mayoral & Jiménez 2011; Jelly *et al.* 2014; Türk *et al.* 2014; Seo *et al.* 2015). The resulting pressure fluctuation p'' is a sum of the two time-dependent effects from overlying turbulence p''_t, and flow-induced capillary pressure p''_c. We assume the capillary pressure is statistically uncorrelated from the stagnation pressure and overlying turbulence. Therefore, r.m.s. fluctuation of capillary pressure is obtained by

$$p''_{c,rms} = \sqrt{p''^2_{rms} - p''^2_{t,rms}}, \tag{6.2}$$

where $p''_{t,rms}$ is the wall pressure fluctuation from overlying turbulence when the interface is flat. $p''_{t,rms}$ is calculated from the DNS data by Seo *et al.* (2015). The total wall pressure fluctuation p'^{+}_{rms}, and each pressure component from stagnation pressure $\tilde{p}^{+}_{rms}$, capillary pressure $p''^{+}_{c,rms}$, and turbulence pressure $p''^{+}_{t,rms}$ are plotted in figure 19.

We do not apply this decomposition method to extract the capillary contribution from the η^+ fluctuation, since decomposition of the turbulence contribution to interface deformation requires solution of the Young–Laplace equation over a smooth wall, in a one-way coupled fashion. This is a more cumbersome postprocessing step than decomposing the pressure data.

Figure 20 presents η^{+}_{rms} and $p''^{+}_{c,rms}$ against the input Weber number We_L for different texture sizes. In figure 20(*a*), η^{+}_{rms} includes all interfacial responses to pressure

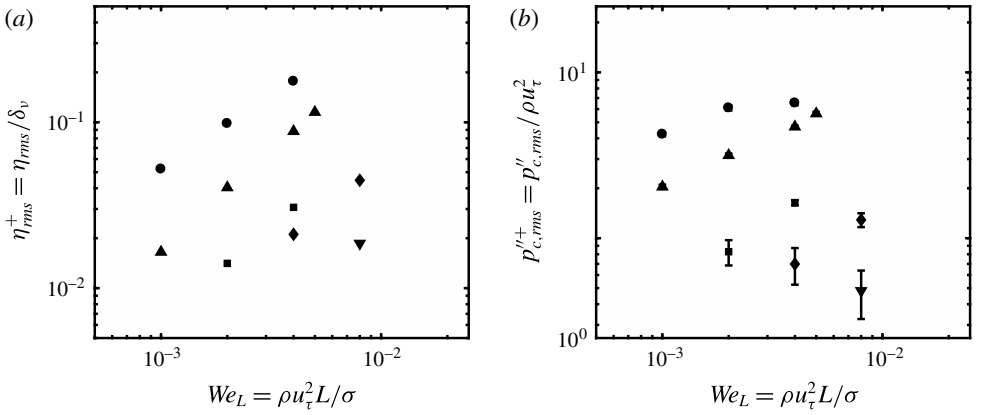

FIGURE 20. Statistics of fluctuations of interface deformation and capillary pressure versus We_L. (*a*) r.m.s. interface deformation in wall units, η^+_{rms}, (*b*) r.m.s. capillary pressure p''^+_c in wall units, ▼: $L^+ \approx 13$, ◆: $L^+ \approx 26$, ■: $L^+ \approx 38$, ▲: $L^+ \approx 77$, ●: $L^+ \approx 155$.

fluctuations from stagnation, capillary waves, and turbulence, while in figure 20(*b*), $p''^+_{c,rms}$ includes only the flow-induced capillary pressure fluctuation. The error bars in figure 20(*b*) are obtained from standard error of mean (SEM) of each p''_{rms} and $p''_{t,rms}$ sampling mean values in subdivided time intervals. Both interface deformations and capillary pressure fluctuations increase with increasing We_L for a fixed L^+; however, they do not collapse for different texture sizes.

Similar to § 4.5, we reconsider what is the most relevant physical quantities for the capillary wave. Again, We_s should be used instead of We_L. Considering input variables We_s, L^+, and U_s^+, we report the best collapsed fit of data to seek the power law for each input variables. We use a linear least squares fit to find the coefficients, a_i, of $\log(p''^+_c) = a_0 + a_1 \log(We_s) + a_2 \log(L^+) + a_3 \log(U_s^+)$, in which We_s, L^+, and U_s^+ values are used for the corresponding p''^+_c data. As a result, a fitting law for the capillary wave is

$$p''^+_{c,rms} \approx 0.06 We_s^{0.57} U_s^{+2.8} L^{+-0.74}, \tag{6.3}$$

as shown in figure 21. We note that the prefactor 0.06 is specifically obtained for $\phi_s = 1/9$. For superhydrophobic surface design purposes, using We^+ is more suitable than using We_s, since it is dependent only on the imposed flow and independent of texture size. Noting that We_s is simply a combination of the non-dimensional parameters of the system, $We_s = We^+ L^+ U_s^{+2}$, the equation (6.3) can be rewritten in terms of wall units as

$$p''^+_{c,rms} \approx 0.06 We^{+0.57} U_s^{+3.9} L^{+-0.17}. \tag{6.4}$$

Equation (6.4) is one of the key results of this study. This equation shows that the capillary pressure has a strong dependency on slip velocity. For cases that the working flow and the flow conditions are prespecified, We^+ would be fixed. However, if the texture size increases, the slip velocity increases accordingly, and the capillary pressure rapidly increases corresponding to the slip velocity.

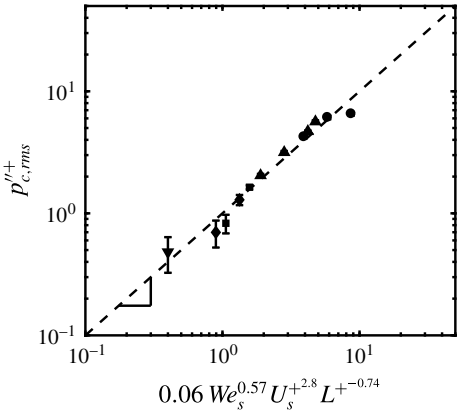

FIGURE 21. Statistics of fluctuations of dimensionless r.m.s. capillary pressure, $p_c^{\prime\prime+}$, versus We_s. ▼: $L^+ \approx 13$, ◆: $L^+ \approx 26$, ■: $L^+ \approx 38$, ▲: $L^+ \approx 77$, ●: $L^+ \approx 155$. – – – –: $p_{c,rms}^{\prime\prime+} \approx 0.06 We_s^{0.57} U_s^{+2.8} L^{+-0.74}$.

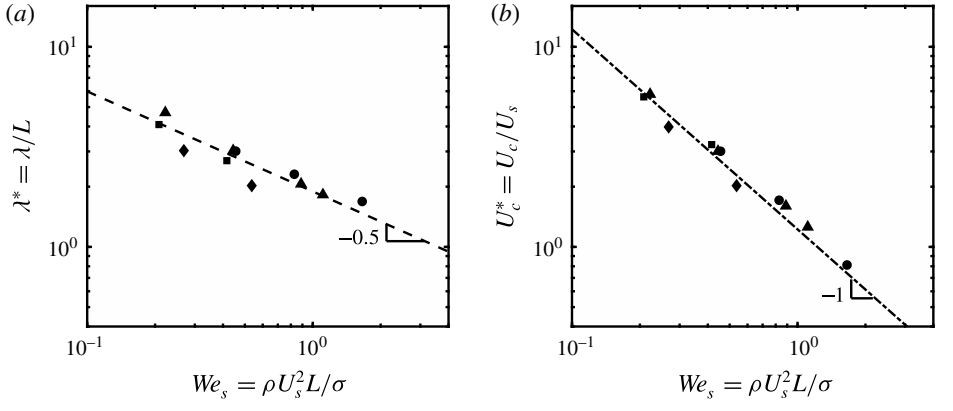

FIGURE 22. Scaling of interfacial quantities scaled in L and U_s versus We_s. (*a*) Wavelength of capillary wave in streamwise direction, λ^*; (*b*) convection velocity of capillary wave, U_c^*. ◆: $L^+ \approx 26$, ■: $L^+ \approx 38$, ▲: $L^+ \approx 77$, ●: $L^+ \approx 155$. – – – –: $\lambda^* \approx 1.9 We_s^{-0.5}$, — · —: $U_c^* \approx 1.2 We_s^{-1}$.

6.2. *Scaling of wavelength and phase speed*

We report scalings as well as fitting coefficients for the estimation of expected behaviour of capillary waves. The log–log scale of data presented in figure 22 reveals that λ^* scales with $We_s^{-0.5}$, and U_c^* scales with We_s^{-1}. The best fit for λ^* is

$$\lambda^* \approx 1.9 We_s^{-0.5}. \tag{6.5}$$

The best fit for phase speed U_c^* measured from DNS data is

$$U_c^* \approx 1.2 We_s^{-1}. \tag{6.6}$$

Both (6.5) and (6.3) are plotted in figure 22.

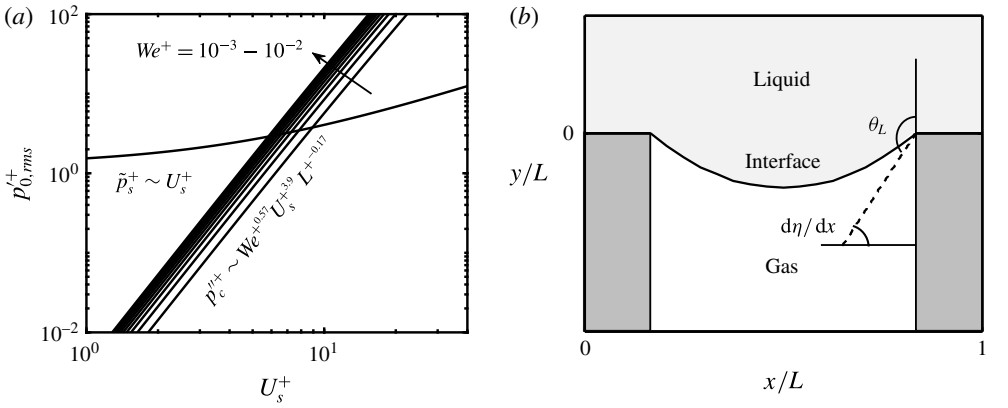

FIGURE 23. (*a*) Scalings of wall pressure fluctuations, $p_{0,rms}^{+}$. $\tilde{p}_s^+$ is wall pressure fluctuation by stagnation pressure, $\tilde{p}_{s,rms}^{+} \approx 0.28U_s^+ + 1.26$ (Seo *et al.* 2015). $p_c''^+$ is wall pressure fluctuation by capillary pressure, $p_{c,rms}''^{+} \approx 0.06We^{+0.57}U_s^{+3.9}L^{+-0.17}$. (*b*) Schematic of example calculation showing interface deformation due to an overlying pressure field. When the slope of the interface at the edge of the post form an angle, θ_L, larger than the advancing contact angle, the interface starts to move.

While We_s is directly measured from DNS in the presented plots, we note that We_s can be predicted *a priori*, given the texture parameters, flow conditions, and fluid properties, from the relation introduced by Seo & Mani (2016), that is $U_s^+ = U_s^+(L^+, \phi_s)$. Specifically they predicted $U_s^+ \sim L^+$ in the small-texture-size limit, and $U_s^+ \sim L^{+1/3}$ for the large-texture-size limit.

7. Implications on design

7.1. *Onset of failure by capillary pressure*

We compare the pressure fluctuations from the stagnation pressure versus capillary pressure as a function of slip velocity in wall units in figure 23(*a*). While previous analysis by Seo *et al.* (2015) suggested a linear scaling of the stagnation pressure with respect to slip velocity, $\tilde{p}_{0,rms}^{+} \approx 0.28U_s^+ + 1.26$, the pressure load imposed by flow-induced capillary waves is $p_{c,rms}''^{+} \approx 0.06We^{+0.57}U_s^{+3.9}L^{+-0.17}$. Therefore, the capillary pressure becomes dominant over stagnation pressure shortly after $U_s^+ \gtrsim 5$, when we consider the surface tension in the practical application regime, $We^+ = 10^{-3}$–10^{-2}.

Similar to Seo *et al.* (2015), we define the onset of failure as the conditions resulting in microscopic contact angles leading to the onset of motion for contact lines. A proper dimensional analysis of the Young–Laplace equation leads to the following scaling law for this failure criterion for interface breakage (Seo *et al.* 2015),

$$p_0'^{+} We^+ L^+ \sim O(1). \tag{7.1}$$

The order one coefficient on the right-hand side of the equation is determined by the failure criteria that the contact angle of gas–liquid interface, $\theta_L = \pi/2 + \tan^{-1}(\mathrm{d}\eta/\mathrm{d}x|_L)$, exceeds the advancing contact angle, θ_{adv}, where $\mathrm{d}\eta/\mathrm{d}x|_L$ is the slope of the gas–liquid interface at the leading edge of the post as shown in figure 23(*b*). Seo *et al.* (2015)

used the self-similar stagnation pressure fields to obtain the $O(1)$ constant on the right-hand side of (7.1) for $\theta_{adv} = 100°$ and 120°. For instance, the resulting relationship for stagnation pressure is $0.28U_s^+We^+L^+ = f(\theta_{adv})$, where f is computed to be equal to 1.7 for $\theta_{adv} = 120°$ and equal to 0.5 for $\theta_{adv} = 100°$. U_s^+ is a known function of L^+ obtained by the scaling introduced in Seo & Mani (2016) as:

$$\frac{(U_s^+\sqrt{\phi_s})}{(0.325 - 0.44\sqrt{\phi_s})} + 0.328(U_s^+\sqrt{\phi_s})^3 = L^+. \tag{7.2}$$

We repeated the same procedure for the capillary waves. Given that the capillary waves observed in DNS have wavelengths larger than the texture size, L, we used a uniform pressure on the textured interface to approximate $f(\theta_{adv}) = O(1)$ constant on the right-hand side of (7.1) for this mechanism. The f constant is computed by measuring the uniform p^+ that leads to deformation angle equal to advancing contact angle. With this simplification the right-hand-side constant is computed to be equal to 0.6 and 0.2, respectively, for $\theta_{adv} = 120°$ and 100°, considering square patterns with $\phi_s = 1/9$. In order to consider the worst case scenario we used the peak of the capillary pressure estimated as $P_{peak} \simeq \sqrt{2}p''_{c,rms}$. The resulting equation for capillary waves with $\theta_{adv} = 120°$ is

$$0.06\sqrt{2}We^{+1.57}U_s^{+3.9}L^{+0.83} = 0.6, \tag{7.3}$$

where the coefficient 0.06 is subject to change with ϕ_s, and U_s^+ can be estimated from (7.2). In appendix B, we discuss the validity of linearization of the Young–Laplace equation to obtain the coefficient on the right-hand side.

7.2. *Boundary map for stable superhydrophobic surface design*

Using the failure mode described in § 7.1, we provide boundary maps for stable drag reduction of superhydrophobic surfaces. The boundary map consists of two independent design parameters: the texture size in wall units, L_c^+, and Weber number in wall units, $We^+ = \mu u_\tau/\sigma$. We will consider multiple contributions to the failure mode, so thus using L^+ and We^+ in design space is suitable while We_s is the controlling parameter only for the capillary pressure. In figure 24(*a*), both criteria from stagnation pressure and capillary pressure fluctuations are represented together. In most of the practical applications of hydrodynamic flows, $We^+ = 10^{-3}$–10^{-2}, and the texture size regime of interest for noticeable drag reduction is $L^+ > 1$. In this regime, the capillary pressure sets a more restrictive boundary than the criterion imposed by the stagnation pressure. The change of slope in each plot indicates transition from $U_s^+ \sim L^+$ to $U_s^+ \sim L^{+1/3}$, respectively, for small and large texture sizes, as discussed by Seo & Mani (2016) and indicated in (7.2). The error bar, indicated by the dashed dotted line in figure 24(*a*), is computed from the error of the fit in figure 21. The 95 % confidence interval of the fit in figure 21 is computed from $1.96\sqrt{\text{mean}[(0.06We_s{}^{0.57}U_s^{+2.8}L^{+-0.74} - p_c''^+)^2 + \text{SEM}(p_c''^+)^2)]}$. This error, translated in the stability diagram, leads to 45 % error in the L_c^+ for $We^+ = 10^{-4}$ and 35 % error in the L_c^+ for $We^+ = 10$.

Next, we include more practical considerations to the presented analysis to make it more relevant to realistic applications. Our recent finding on the effect of texture randomness (Seo & Mani 2017) indicates that the maximum deformation angle of the randomly distributed textured superhydrophobic surface is approximately twice

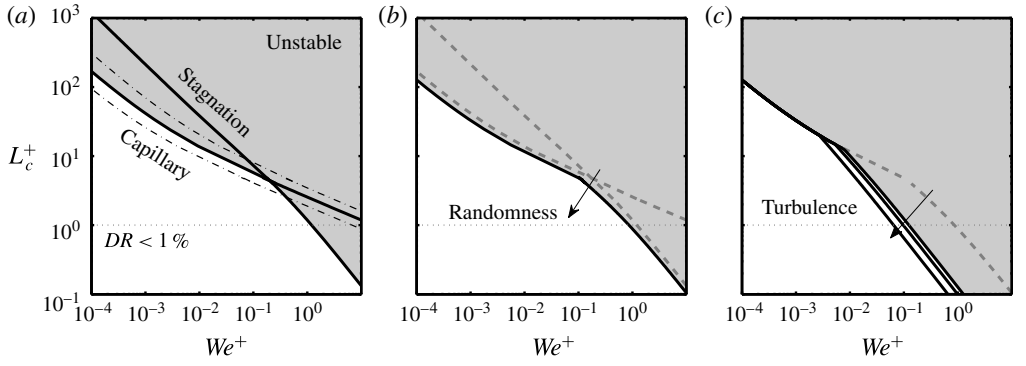

FIGURE 24. Design map for the stable drag reduction of superhydrophobic surfaces in turbulent flows. L_c^+ is the maximum allowable texture size for stable drag reduction. $We^+ = \mu u_\tau/\sigma$ is Weber number based on inner scaling. The grey area is the unstable region and the white area is the stable region. (*a*) Shows the stability criteria imposed by stagnation pressure and capillary pressure. The dashed-dot lines are error bounds of the estimation of stability boundary for capillary pressure. (*b*) Shows the effect of texture randomness on the total stability region. Dashed lines are stability criteria imposed by stagnation pressure and capillary pressure for aligned posts. (*c*) Shows the effect of turbulence pressure on the total stability region. Dashed line is the solid curve in panel (*b*). Three different lines are plotted from different confidence intervals for pressure variation: 95 % (*c*), 99 % (*b*), 99.99 % (*a*). The area below the dotted lines indicates the region where *DR* is less than 1 %. All analyses use the advancing contact angle $\theta_{adv} = 120^\circ$ with the solid fraction of $\phi_s = 0.11$.

that of the perfectly aligned posts considered in this study. For randomly distributed textured superhydrophobic surfaces, produced by spray coating or an etched process, this geometric randomness will push the boundaries imposed by our analysis from aligned, periodic textured superhydrophobic surfaces as shown in figure 24(*b*).

Moreover, the stability region will be further shrunk when we consider unsteady, intermittent turbulence pressure fluctuations in addition to the stagnation pressure and capillary pressure. The worst scenario for the interface stability can occur instantaneously when some of travelling turbulence pressure with high-intensity encounters an interface. An instantaneous local turbulence pressure fluctuation can be estimated by multiplication of 1.96 on $p''^+_{t,rms}$ with 95 % confidence. We consider the multiplier 2.58 for 99 % confidence and 4.0 for 99.99 % confidence and the effect of using different confidence intervals is shown in figure 24(*c*). Here we avoid a higher number of digits in the confidence interval since the extremely rare high-pressure events are local in space and time (unlike capillary waves that have large features). Therefore, although they can cause instant deformation of the interface, it is unclear whether they lead to failure, as they may not persist long enough over a significant portion of a texture. In this analysis we use $p''^+_{t,rms} \approx 3$, which has been observed in DNS of turbulent channel flow up to $Re_\tau \approx 5000$ (Lee & Moser 2015). Our previous analysis has shown that the turbulence pressure fluctuation from overlying turbulent flows in the presence of texture, $p''^+_{t,rms}$, is marginally modified from a conventional smooth channel flow (Seo *et al.* 2015). Higher Reynolds number involves slightly higher $p''^+_{t,rms}$ with a logarithmic dependence on Re_τ. As an example, a case with extremely large $Re_\tau = 5 \times 10^5$ would lead to $p''^+_{t,rms} \approx 4.5$ (Farabee & Casarella 1991). This modification is smaller than the uncertainty associated with the discussed

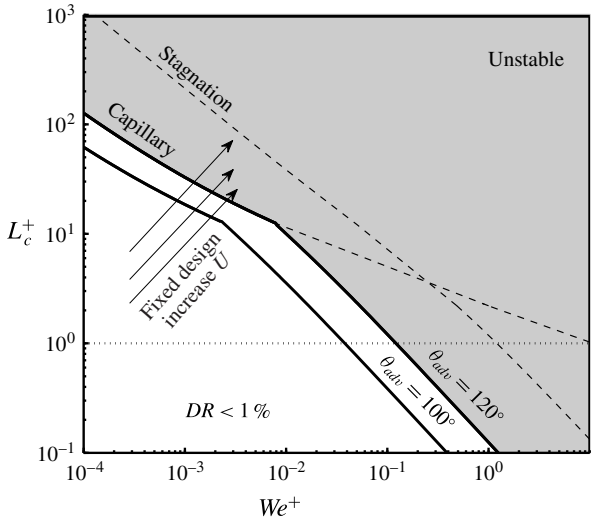

FIGURE 25. Total design map for the stable drag reduction of superhydrophobic surfaces in turbulent flows. L_c^+ is the maximum allowable texture size for stable drag reduction. $We^+ = \mu u_\tau/\sigma$ is Weber number based on inner scaling. Arrows indicate the variability of stability of gas pockets when increasing velocity fixing fluid and design parameters. The upper solid line uses $\theta_{adv} = 120°$, and the bottom solid line uses $\theta_{adv} = 100°$ in the analysis of the failure mechanisms. Dashed lines are the failure boundaries imposed by stagnation and capillary pressure fluctuations. The dotted line is a boundary below which the drag reduction is expected to be under 1 %. The boundary map is obtained for the solid fraction $\phi_s = 0.11$ and 95 % confidence level for the effect of turbulence pressure.

precision of the confidence interval. With these considerations, the boundary map, between stable and unstable designs, in figure 24(*c*) shows the stable design spaces, considering all of the aforementioned effects.

In summary, we recap the design criteria for stable drag reduction in figure 25. If the speed of overlying flow, U, increases for fixed design parameters and fluid properties (L, ϕ_s, σ, ρ, μ), the viscous length, δ_v, decreases, leading to a proportional increase in both L^+ and We^+, and thus the state in the design map would move along the 45° line up and to the right, as indicated by the arrows in figure 25. The maximum allowable drag reduction can be estimated by the shifted-TBL model and a phenomenological model for slip length suggested by Seo & Mani (2016) for the critical texture size in figure 25. We note that drag reduction is not only a function of slip length, but subject to change with Reynolds number. In this particular case we consider a scenario when the solid fraction is $\phi_s = 1/9$ and $Re_\tau \approx 5000$ for the estimation of drag reduction. The critical texture length in figure 25 shows that the maximum allowable drag reduction in a realistic superhydrophobic surface with flow condition $We^+ = 10^{-3}$–10^{-2} would be approximately from 15 % to 45 % for the best chemically coated superhydrophobic surfaces with the maximum microscopic contact angle of $\theta_{adv} = 120°$. If a superhydrophobic surface has a different chemistry which lowers the advancing contact angle, e.g. $\theta_{adv} = 100°$, the boundary would be further pushed downwards, limiting the maximum allowable drag reduction from ≈45 % to 30 % at $We^+ \approx 10^{-3}$. The overall prediction of the maximum stable drag reduction by our analysis is consistent with current experimental observations, in which most

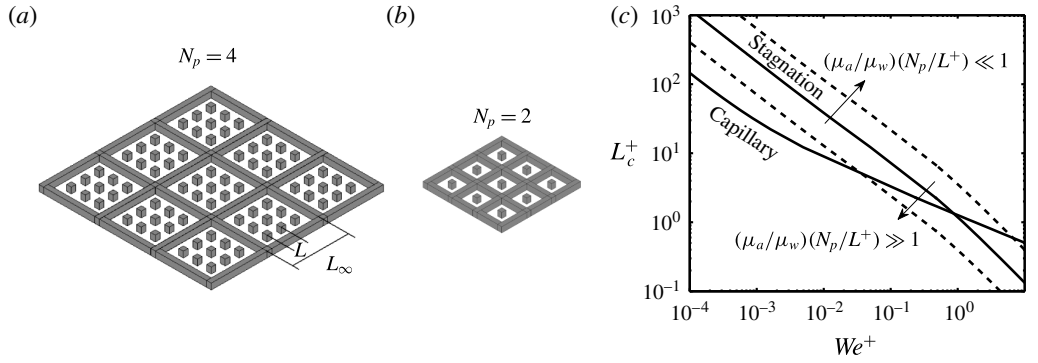

FIGURE 26. Schematic representations of barriers to prevent the shear-driven drainage and stability criteria. L is pattern period of post arrays, L_∞ is period of barriers, and N_p is the number of periods in a barrier, $N_p = L_\infty/L$. (*a*) Posts enclosed by barriers with $N_p = 4$, (*b*) posts enclosed by barriers with $N_p = 2$. (*c*) Change of stability criteria according to the relative importance of shear-driven failure mechanism to stagnation pressure failure mechanism. μ_a is viscosity of air, μ_w is viscosity of water, L^+ is pattern period in wall units. Dashed lines are predicted stability boundaries imposed by shear-driven failure depending on the ratio between stagnation and shear-driven pressure.

successful drag reductions were limited to be approximately less than 30 % (Bidkar *et al.* 2014; Haibao *et al.* 2015; Srinivasan *et al.* 2015; Zhang *et al.* 2015).

7.3. *Considerations of failure due to shear-driven drainage*

An additional failure mechanism for superhydrophobic surfaces is shear-driven drainage (Wexler *et al.* 2015*b*; Liu *et al.* 2016). Wexler *et al.* (2015*a*) proposes a remedy for the shear-driven drainage, by installing barriers with finite periodicity which should be smaller than or equal to a threshold length, L_∞, that can retain the enclosed fluid. Two examples of such barriers with different barrier periodicity defined by $N_p = L_\infty/L$, are portrayed in figure 26(*a*,*b*). According to Wexler *et al.* (2015*b*), the threshold length for shear-driven drainage is $\sim O(1)\sigma\gamma h/\tau_{yx}$, where h is the height of the texture, τ_{yx} is the imposed shear on top of the cavity, and γ is the curvature of the interface. Assuming the texture height is $\sim L$, the shear-driven pressure that can balance the capillary pressure, $\sigma\gamma$, would then be $p_{shear} \sim O(1)\mu_{air}U_s N_p/L$. Considering the stagnation pressure scales as $p_{stagnation} \sim 0.28\mu_{water}U_s/\delta_v$ (Seo *et al.* 2015), the ratio between the shear-driven pressure to the stagnation is

$$\frac{p_{shear}}{p_{stagnation}} \sim \frac{\mu_{air}N_p}{\mu_{water}L^+}. \tag{7.4}$$

For superhydrophobic surfaces, due to the low viscosity ratio of air to water, $\mu_{air}/\mu_{water} \approx 2\,\%$, this ratio remains small if N_p is on the order of 10 or smaller. When N_p is comparable to the viscosity ratio, the shear-driven pressure will dominate the stagnation pressure.

In figure 26(*c*), we show the rough estimate of the change of the stability boundary according to the ratio between the shear-driven pressure and the stagnation pressure. When the number of periods within barriers, N_p, becomes large, the shear-driven failure will be the dominant mechanism for the interface breakage. The optimal

choice of N_p is required since small N_p ensures stable gas pockets from shear-driven drainage, but it also suppresses the drag reduction due to additional solid–liquid contact area. For example, an extremely small $N_p = 1$ formulates shear-free holes with periodicity, L, which separately contain air pockets. While this configuration may consist a highly robust design for superhydrophobic surfaces, the drag reduction is significantly impacted. Our preliminary results show isolated holes can lead to half the drag reduction compared to posts with the same $\phi_s = 1/9$. Based on the scaling analysis of (7.4) we estimate that $N_p \sim O(10)$ provides a good compromise between robustness and drag reduction for superhydrophobic surfaces subject to turbulent flows.

8. Summary and conclusion

We presented an investigation of the dynamic behaviour of gas–liquid interfaces on a superhydrophobic surface in response to hydrodynamic turbulence in an overlying flow. DNS of turbulent channel flows over a wide range of parameters were developed to perform this investigation. The DNS take into account the physics of superhydrophobic surface via patterned slip/no-slip boundary conditions on the overlying flow, and deformability of the air–water interface via a linearized Young–Laplace equation. Our investigations identified flow-induced capillary waves as a mechanism where turbulence can energize capillary modes in the form of streamwise coherent waves that travel upstream. While kinematic statistics, such as slip length, are not sensitive to the presence of capillary waves, the pressure fields are strongly affected by these modes. Via various analyses, including identification of scalings for data collapse and semianalytical linear inviscid analysis, we developed insights into the behaviour of flow-induced capillary waves.

The knowledge gained from investigation of DNS data led to the development of threshold criteria for the failure of superhydrophobic surfaces under realistic conditions. To this end, the onset of contact line movement was used to quantify a failure condition, leading to the boundary maps between stable and unstable zones in We^+ versus L^+ parameter space, considering various contact angle scenarios. A major contribution of this paper is the presentation of an overview of other failure modes that have been identified in recent literature in the context of the developed parameter maps. Namely, we considered failure due to stagnation pressure (studied by Seo *et al.* 2015), and found that this mode is the critical limiter of stability only in the limit of very large We^+; for typical We^+ values, robustness of air pocket retention is more critically limited by the capillary pressure modes discussed in the present study. However, direct evidence of these failure modes should be provided by experiment. Additionally, we presented an overview of the shear-driven drainage mechanism (Wexler *et al.* 2015*b*) and identified the conditions under which this mechanism may compete with the other two mechanisms in limiting the robustness of air retention. Specifically, the shear-driven drainage is not the limiting mechanism as long as the height of the posts is not small compared to the pattern wavelength, and as long as gas pockets are kept isolated with barriers distanced within tens of pattern wavelengths.

Considering a solid fraction of $\phi_s \approx 0.11$, and including the overall contribution of all identified mechanisms of failure, we estimate that maximum possible drag reduction in the turbulent flow regime to be in the range 45 % to 15 % for Weber numbers from 10^{-3} to 10^{-2} in wall units for a surface microscopic contact angle of 120°. The maximum drag reduction decreases from 45 % to 30 % in the case of a

surface microscopic contact angle of 100° for $We^+ = 10^{-3}$. This result is consistent with the experimental measurements of drag reduction by superhydrophobic surfaces. While increasing ϕ_s is likely to shrink the unstable zones in the developed design maps, surfaces with larger ϕ_s result in less drag reduction; the impact of varying ϕ_s on the prefactor of the developed scalings should be studied in a future investigation.

A number of extensions and improvements to the present work can be envisioned.

(i) While reasonable understanding of the dispersion relation governing the induced capillary waves is provided, it is still unclear how turbulence decides which capillary modes to excite. It is also unclear why this excitement dominantly involves a compact representation of capillary modes. To this end, various analysis techniques such as the resolvent technique (McKeon & Sharma 2010; McKeon, Sharma & Jacobi 2013) or its variants adopted for non-rigid surfaces (Luhar, Sharma & McKeon 2015, 2016) may be the most suitable technique to consider.

(ii) Considering realistic surfaces that typically involve random posts, it is useful to extend the present DNS investigations to the case of surfaces with randomly distributed posts. In the limit of a flat interface, Seo & Mani (2017) investigated the effects of randomness and quantified their impact on increased maximum stagnation pressure and deterioration of drag-reduction performance. In the figures presented in § 7, the same trends were hypothesized for the capillary wave mechanism, but confirming this hypothesis requires a thorough and original investigation.

(iii) The presented analysis is based on a linearized interface model which is only useful for the prediction of onset of nonlinear events. Extension of DNS to fully coupled two-phase flows with appropriate contact line models can shed light into processes that lead to full bubble drainage and perturbations beyond the discussed early onsets.

(iv) The analysis presented here considers an ideal scenario where all texture posts have the same height; realistic surfaces are likely to introduce rough interfaces, even in the complete Cassie–Baxter state. The form drag induced by interfacial roughness further lowers the performance in drag reduction (Ling *et al.* 2016) and may also affect the instability threshold. An extension of the presented analysis to rough superhydrophobic surfaces can provide useful insights into the competition between performance and robustness under such conditions.

(v) The effects of static pressure and mean pressure gradient were not considered in the current analysis. We assumed a scenario of applications of superhydrophobic surfaces where within each block between barriers the air pressure balances the static pressure of the overlaying fluid. The variation of streamwise pressure due to mean pressure gradient is assumed negligible, if the barrier size is smaller than the boundary layer thickness, such as $p'^+ \approx (\mathrm{d}\overline{p}/\mathrm{d}x)^+ L_\infty^+ \lesssim 1$, which is less than pressure fluctuations from overlying turbulence.

Acknowledgements

This work was supported by the Office of Naval Research under grant 3002451214. The program officer is K.-H. Kim. The authors greatly appreciate the Kwanjeong Educational Foundation for the funding support for J.S.

Supplementary movies

Supplementary movies are available at https://doi.org/10.1017/jfm.2017.733.

Appendix A. Energy absorption by viscous effects in the gas layer

For textures whose height is on the order of their width, the ratio of energy absorption by the gas layer to that absorbed by the surface tension scales as

$$\epsilon_g \sim \left(\frac{\mu_{gas}}{\mu_{liquid}}\right) We^+ L^+ \omega^+, \tag{A 1}$$

where ω^+ is the frequency of the capillary waves. In the settings considered here, We^+L^+ is much less than unity and always less than $O(1)$, and ω^+ is either $O(1)$ or mostly smaller than unity as shown in figure 15(*b*) for the capillary wave period in wall units. Given that μ_{air}/μ_{water} is much smaller than unity, the viscous effects in the gas are negligible.

Appendix B. Linearization on the gas–liquid interface

B.1. *Accuracy of linearization of the Young–Laplace equation*

We discuss the validity of the linearized boundary condition for a gas–liquid interface in our study and report errors of using it against the Young–Laplace equation without linearization. The nonlinear Young–Laplace equation equates pressure difference across the interface and curvature of the interface,

$$\frac{\dfrac{\partial^2\eta}{\partial x^2}\left(1+\dfrac{\partial\eta}{\partial z}\right)+\dfrac{\partial^2\eta}{\partial z^2}\left(1+\dfrac{\partial\eta}{\partial x}\right)-2\dfrac{\partial\eta}{\partial x}\dfrac{\partial\eta}{\partial z}\dfrac{\partial^2\eta}{\partial x\partial z}}{\left(1+\left(\dfrac{\partial\eta}{\partial x}\right)^2+\left(\dfrac{\partial\eta}{\partial x}\right)^2\right)^{3/2}} \approx \frac{P_{liquid}-P_{gas}}{\sigma}. \tag{B 1}$$

The linearized Young–Laplace equation (2.4) is the first-order approximation of (B 1) if the slope of the interface is assumed smaller than unity, $(\partial\eta/\partial x, \partial\eta/\partial z) \ll 1$.

We additionally conducted a simulation resulting in the largest deformation $P155W4$ in table 1 by using the Young–Laplace equation without linearization. The simulation was run for more than a 15 eddy turnover time, and the last 12 eddy turnover time data were used and averaged for statistics. The error of DNS results using the linearized Young–Laplace equation against the Young–Laplace without linearization for mean convection velocity (U_c^+), time period (T^+), and wavelength of capillary wave (λ^+) are 2.6 %, 0.3 % and 2.7 %. The root-mean-square error for pressure fluctuation is less than 3 % and the error for r.m.s. interface deformation is 3.3 %. Since all errors associated with linearization are under 4 % for the largest deformation case, we expect all other cases with smaller We_s are not affected by the linearization.

We examined the error of using the linearized Young–Laplace equation to determine the onset condition of failure by capillary waves, introduced in § 7.1. In the case of a moving contact angle of 120°, the Young–Laplace equation without linearization predicts an 11 % smaller critical texture size than the prediction from the linearized Young–Laplace equation. The right-hand-side coefficient of the (7.3) is then reduced by 11 %. For the system where the moving contact angle is 100° this error reduces to less than 1 %. The remaining conclusion on the design map is marginally changed by this correction for linearization since the key factor for determining onset is a rapid increase of slip velocity and an order one change with respect to We^+.

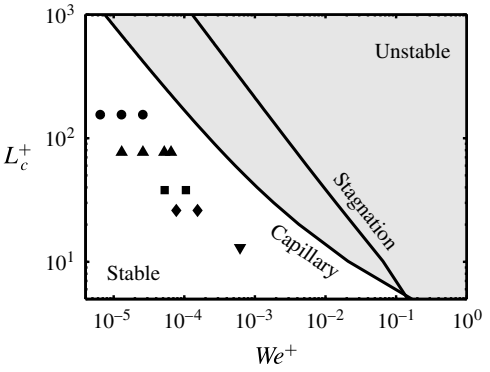

FIGURE 27. Representation of DNS parameters on the design map. ▼: $L^+ \approx 13$, ◆: $L^+ \approx 26$, ■: $L^+ \approx 38$, ▲: $L^+ \approx 77$, ●: $L^+ \approx 155$.

B.2. *Accuracy of linearization of the kinematic condition*

The leading error associated with linearization of the kinematic boundary condition, equation (2.7), is second-order $O(\eta^2)$, neglecting the leading $(\eta^2/2)(\partial^2 v/\partial y^2)|_{y=\eta}$ term. The most deformed case is simulation $P155W4$ in table 1, where the r.m.s. deformation is 0.1 in wall units, and in this case the leading-order error term is on the order of 10^{-2}. The resulting error is less than 10 % for wall-normal velocities.

B.3. *Regime of parameters in current study*

We note that the current simulations are conducted in a stable operation of superhydrophobic surfaces keeping gas pockets safe. The predicted onset failure used the projection of scalings from well-collapsed DNS data. In figure 27, we plot our simulation parameters on a design map. Although We^+ in current study is smaller than the practical regime of interest, the range of We_s considered in this study, $0.2 \lesssim We_s \lesssim 1.7$, matches with realistic cases. Plugging in values in a realistic operating condition, $\rho = 1000$ kg m^{-3}, $L \approx 50$ μm, $\sigma = 0.071$ N m^{-1}, $U_s \approx 3u_\tau$, where $u_\tau \approx 0.3$ m s^{-1} for $U_\infty = 10$ m s^{-1}, We_s would be approximately 0.7, which is in the middle of span for We_s in this study. In practice L^+ tends to be smaller (requiring expensive DNS) and We^+ tends to be larger, leading to similar We_s ranges to those considered here.

Appendix C. Verification of the code with a perturbation problem with deformable interface

We consider a perturbation problem where one wall is fully covered by a gas–liquid interface with a finite surface tension. We use normal modes, which consists of introducing sinusoidal disturbances on a basic state. In this way we compare simulations against analytical solutions for different modes of perturbation. On the base state described by $\boldsymbol{U} = (U, 0, 0)$, we superpose a disturbance of the form

$$q(x, y, z, t) = \hat{q}(y) \exp(\omega t + \mathrm{i}k_x x + \mathrm{i}k_z z), \tag{C 1}$$

where q represents the perturbed quantities $(u, v, w; p)$. We consider all real wavenumbers (k_x, k_z) in a periodic x–z domain. The physical solutions described by (C 1) can be obtained by computing the real part of the complex fields. We

assume the perturbation amplitude is much smaller than the background velocity, $u, v, w \ll U$. The continuity equation (2.1) is then

$$\boldsymbol{D} \cdot \hat{\boldsymbol{u}} = 0, \tag{C 2}$$

where $\boldsymbol{D} = (\mathrm{i}k_x, \partial_y, \mathrm{i}k_z)$, and momentum equation (2.2) becomes

$$(\omega + \mathrm{i}k_x U)\hat{\boldsymbol{u}} = -\frac{1}{\rho}\boldsymbol{D}\hat{p} + \nu(-\tilde{k}^2 + \partial_y^2)\hat{\boldsymbol{u}}, \tag{C 3}$$

where $\tilde{k} = \sqrt{k_x^2 + k_z^2}$. At the boundary, we use the linearized Young–Laplace equation,

$$\hat{p}_{y=0} = -\sigma\tilde{k}^2\hat{\eta}, \tag{C 4}$$

and the kinematic condition on the interface (2.7),

$$v_{y=0} = (\omega + \mathrm{i}k_x U)\hat{\eta}, \tag{C 5}$$

as boundary conditions at $y = 0$, where $\eta(x, z) = \hat{\eta}\exp(\omega t + \mathrm{i}k_x x + \mathrm{i}k_z z)$. Note that the velocity and pressure fields are fully coupled with the deformation of interface. By solving the equations from (C 1) to (C 5) together with the shear-free condition (2.3), a solution for time frequency is obtained as

$$\omega = -\mathrm{i}k_x U - \nu\tilde{k}^2 \pm \sqrt{\nu^2\tilde{k}^4 - \sigma\tilde{k}^3}, \tag{C 6}$$

where the first term in the time frequency represents the advection of the solution with background velocity. The remaining real part of the solution is the decay rate, while the imaginary part of the solution is oscillation due to the surface tension effect. The real form of the solution is

$$q(x, y, z, t) = \hat{q}(y)\exp\left(\left(-\nu\tilde{k}^2 \pm \sqrt{\nu^2\tilde{k}^4 - \sigma\tilde{k}^3}\right)t\right)\cos(k_x(x - Ut))\cos(k_z z), \tag{C 7}$$

when $\nu^2\tilde{k} - \sigma \geqslant 0$,

$$q(x, y, z, t) = \hat{q}(y)\exp(-\nu\tilde{k}^2 t)\cos\left(t\sqrt{\sigma\tilde{k}^3 - \nu^2\tilde{k}^4}\right)\cos(k_x(x - Ut))\cos(k_z z), \tag{C 8}$$

when $\nu^2\tilde{k} - \sigma < 0$.

The full solution fields for $\hat{q}(y)$ are

$$\hat{u} = \frac{\nu k_x(m^2 + \tilde{k}^2)}{\mathrm{i}\tilde{k}}\left(\mathrm{e}^{-\tilde{k}y} - \left(\frac{2m\tilde{k}}{m^2 + \tilde{k}^2}\right)\mathrm{e}^{-my}\right)\hat{\eta}, \tag{C 9}$$

$$\hat{v} = \nu(m^2 + \tilde{k}^2)\left(\mathrm{e}^{-\tilde{k}y} - \left(\frac{2\tilde{k}^2}{m^2 + \tilde{k}^2}\right)\mathrm{e}^{-my}\right)\hat{\eta}, \tag{C 10}$$

$$\hat{p} = -\rho\sigma\tilde{k}^2\mathrm{e}^{-\tilde{k}y}\hat{\eta}, \tag{C 11}$$

and $\hat{w} = (k_z/k_x)\hat{u}$, where $m = (\tilde{k}^4 - \sigma\tilde{k}^3/\nu^2)^{1/4}$.

We verified our code against the above analytical solution of the diffusion–oscillation–advection problem, in which the interface responds to the overlying fluid motion. Our numerical scheme for deformable interface fully coupled with the overlying flow can capture the motion of an interface with the given surface tension. We compare our numerical results with analytical solutions when $\sigma = U = 1$, $k_x = k_z = 8$, $\nu = 0.1$ in figures 28 and 29.

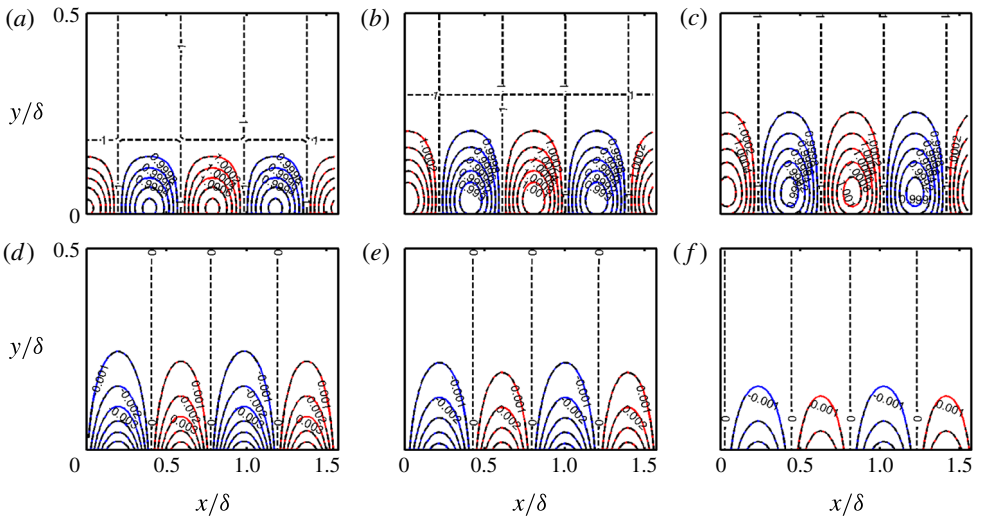

FIGURE 28. (Colour online) Streamwise velocity (*a–c*) and pressure (*d–f*) snapshots in $z/\delta = 0$ at time $tU/\delta = 0$, 0.02, 0.04, respectively. Blue and red solid lines are from numerical simulations, and black dashed lines are analytical solutions (C 9), (C 11). Blue line is for negative values, and red line is for positive values.

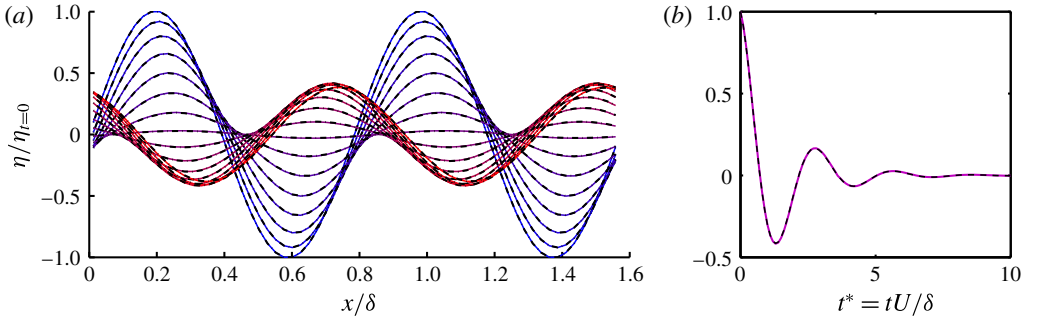

FIGURE 29. (Colour online) Time evolution of interface location normalized by its initial magnitude. (*a*) Oscillation–diffusion–advection of gas–liquid interface. From blue to red, the lines are from time snapshots in $tU/\delta = 0$–1.5 with a time interval 0.1. (*b*) A trace of a peak point in the initial condition. The solid magenta line is the numerical solution. For both plots, dashed-dot lines are analytical solutions.

REFERENCES

ALJALLIS, E., SARSHAR, M. A., DATLA, R., SIKKA, V. & JONE, A. 2013 Experimental study of skin friction drag reduction on superhydrophobic flat plates in high Reynolds number boundary layer flow. *Phys. Fluids* **25**, 025103.

BIDKAR, R. A., LEBLANC, L., KULKARNI, A. J., BAHADUR, V., CECCIO, S. L. & PERLIN, M. 2014 Skin-friction drag reduction in the turbulent regime using random-textured hydrophobic surfaces. *Phys. Fluids* **26**, 085108.

BUSSE, A. & SANDHAM, N. D. 2012 Influence of an anisotropic slip-length boundary condition on turbulent channel flow. *Phys. Fluids* **24**, 055111.

BYUN, D., KIM, J., KO, H. S. & PARK, H. C. 2008 Direct measurement of slip flows in superhydrophobic microchannels with transverse grooves. *Phys. Fluids* **20**, 113601.

CASSIE, A. B. D. & BAXTER, S. 1944 Wettability of porous surfaces. *Trans. Faraday Soc.* **40**, 546–551.

CHOI, C.-H. & KIM, C.-J. 2006 Large slip of aqueous liquid flow over a nanoengineered superhydrophobic surface. *Phys. Rev. Lett.* **96**, 066001.

CHOI, H. & MOIN, P. 1990 On the spacetime characteristics of wallpressure fluctuations. *Phys. Fluids* **2**, 1450–1460.

CHOI, H., MOIN, P. & KIM, J. 1993 Direct numerical simulation of turbulent flow over riblets. *J. Fluid Mech.* **255**, 503–539.

DANIELLO, R., WATERHOUSE, N. E. & ROTHSTEIN, J. P. 2009 Turbulent drag reduction using superhydrophobic surfaces. *Phys. Fluids* **21**, 085103.

DAVIS, A. M. J. & LAUGA, E. 2009 Geometric transition in friction for flow over a bubble mattress. *Phys. Fluids* **21**, 011701.

DAVIS, A. M. J. & LAUGA, E. 2010 Hydrodynamic friction of fakir-like superhydrophobic surfaces. *J. Fluid Mech.* **661**, 402–411.

FARABEE, T. M. & CASARELLA, M. J. 1991 Spectral features of wall pressure fluctuations beneath turbulent boundary layers. *Phys. Fluids* A **3**, 2410–2420.

FUKAGATA, K., KASAGI, N. & KOUMOUTSAKOS, P. 2006 A theoretical prediction of friction drag reduction in turbulent flow by superhydrophobic surfaces. *Phys. Fluids* **18**, 051703.

GARCÍA-MAYORAL, R. & JIMÉNEZ, J. 2011 Hydrodynamic stability and breakdown of the viscous regime over riblets. *J. Fluid Mech.* **678**, 317–347.

GOLOVIN, K. B., GOSE, J. W., PERLIN, M., CECCIO, S. L. & TUTEJA, A. 2016 Bioinspired surfaces for turbulent drag reduction. *Phil. Trans. R. Soc. Lond.* A **374**, 20160189.

HAIBAO, H., PENG, D., FENG, Z., DONG, S. & YANG, W. 2015 Effect of hydrophobicity on turbulent boundary layer under water. *Exp. Therm. Fluid Sci.* **60**, 148–156.

HYVÄLUOMA, J. & HARTING, J. D. R. 2008 Slip flow over structured surfaces with entrapped microbubbles. *Phys. Rev. Lett.* **100**, 246001.

JELLY, T. O., JUNG, S. Y. & ZAKI, T. A. 2014 Turbulence and skin friction modification in channel flow with streamwise-aligned superhydrophobic surface texture. *Phys. Fluids* **26**, 095102.

JUNG, T., CHOI, H. & KIM, J. 2016 Effects of the air layer of an idealized superhydrophobic surface on the slip length and skin-friction drag. *J. Fluid Mech.* **790**, R1.

KARATAY, E., HAASE, A. S., VISSER, C. W., SUN, C., LOHSE, D., TSAIA, P. A. & LAMMERTINK, R. G. H. 2013 Control of slippage with tunable bubble mattresses. *Proc. Natl Acad. Sci.* **110** (21), 8422–8426.

KIM, E. & CHOI, H. 2014 Space–time characteristics of a compliant wall in a turbulent channel flow. *J. Fluid Mech.* **756**, 30–53.

KIM, J. 1988 On the structure of pressure fluctuations in simulated turbulent channel flow. *J. Fluid Mech.* **205**, 421–451.

KIM, J. & HUSSAIN, F. 1993 Propagation velocity of perturbations in turbulent channel. *Phys. Fluids* **5**, 695–706.

KIM, J. & MOIN, P. 1985 Application of a fractional step method to incompressible Navier–Stokes equations. *J. Comput. Phys.* **59**, 308–323.

LEE, C., CHOI, C.-H. & KIM, C.-J. 2008 Structured surfaces for a giant liquid slip. *Phys. Rev. Lett.* **101**, 064501.

LEE, C. & KIM, C.-J. 2009 Maximizing the giant liquid slip on superhydrophobic microstructures by nanostructuring their sidewalls. *Langmuir* **25**, 12812–12818.

LEE, C. & KIM, C.-J. 2011 Influence of surface hierarchy of superhydrophobic surfaces on liquid slip. *Langmuir* **27**, 4243–4248.

LEE, J., JELLY, T. O. & ZAKI, T. A. 2015 Effect of Reynolds number on turbulent drag reduction by superhydrophobic surface textures. *Flow Turbul. Combust.* **95**, 277–300.

LEE, M. & MOSER, R. D. 2015 Direct numerical simulation of turbulent channel flow up to $Re_\tau = 5200$. *J. Fluid Mech.* **774**, 395–415.

LI, Y., ALAME, K. & MAHESH, K. 2017 Feature-resolved computational and analytical study of laminar drag reduction by superhydrophobic surfaces. *Phys. Rev. Fluids* **2**, 054002.

LING, H., SRINIVASAN, S., GOLOVIN, K., MCKINLEY, G. H., TUTEJA, A. & KATZ, J. 2016 High-resolution velocity measurement in the inner part of turbulent boundary layers over super-hydrophobic surfaces. *J. Fluid Mech.* **801**, 670–703.

LIU, Y., WEXLER, J. S., SCHÖNECKER, C. & STONE, H. A. 2016 Effect of viscosity ratio on the shear-driven failure of liquid-infused surfaces. *Phys. Rev. Fluids* **1**, 074003.

LUHAR, M., SHARMA, A. S. & MCKEON, B. J. 2015 A framework for studying the effect of compliant surfaces on wall turbulence. *J. Fluid Mech.* **768**, 415–441.

LUHAR, M., SHARMA, A. S. & MCKEON, B. J. 2016 On the design of optimal compliant walls for turbulence control. *J. Turbul.* **17**, 787–806.

MARTELL, M. B., PEROT, J. B. & ROTHSTEIN, J. P. 2009 Direct numerical simulations of turbulent flows over superhydrophobic surfaces. *J. Fluid Mech.* **620**, 31–41.

MARTELL, M. B., ROTHSTEIN, J. P. & PEROT, J. B. 2010 An analysis of superhydrophobic turbulent drag reduction mechanisms using direct numerical simulation. *Phys. Fluids* **22**, 065102.

MCKEON, B. J. & SHARMA, A. S. 2010 A critical-layer framework for turbulent pipe flow. *J. Fluid Mech.* **658**, 336–382.

MCKEON, B. J., SHARMA, A. S. & JACOBI, I. 2013 Experimental manipulation of wall turbulence: a systems approach. *Phys. Fluids* **25**, 031301.

MIN, T. & KIM, J. 2004 Effects of hydrophobic surface on skin-friction drag. *Phys. Fluids* **16**, L55–L58.

MORINISHI, Y., LUND, T. S., VASILYEV, O. V. & MOIN, P. 1998 Fully conservative higher order finite difference schemes for incompressible flow. *J. Comput. Phys.* **143**, 90–124.

MOSER, R., KIM, J. & MANSOUR, N. 1998 Direct numerical simulation of turbulent channel flow up to $Re_\tau \approx 590$. *Phys. Fluids* **11**, 943–945.

OU, J., PEROT, J. B. & ROTHSTEIN, J. P. 2004 Laminar drag reduction in microchannels using ultrahydrophobic surfaces. *Phys. Fluids* **16**, 4635–4643.

OU, J. & ROTHSTEIN, J. P. 2005 Direct velocity measurements of the flow past drag-reducing ultrahydrophobic surfaces. *Phys. Fluids* **17**, 13606.

PARK, H., PARK, H. & KIM, J. 2013 A numerical study of the effects of superhydrophobic surface on skin-friction drag in turbulent channel flow. *Phys. Fluids* **25**, 110815.

PARK, H., SUN, G. & KIM, C.-J. 2014 Superhydrophobic turbulent drag reduction as a function of surface grating parameters. *J. Fluid Mech.* **747**, 722–734.

PATANKAR, N. A. 2010 Consolidation of hydrophobic transition criteria by using an approximate energy minimization approach. *Langmuir* **26**, 8941–8945.

PIAO, L. & PARK, H. 2015 Two-dimensional analysis of air–water interface on superhydrophobic grooves under fluctuating water pressure. *Langmuir* **31**, 8022–8032.

RASTEGARI, A. & AKHAVAN, R. 2015 On the mechanism of turbulent drag reduction with super-hydrophobic surfaces. *J. Fluid Mech.* **773**, R4.

REYNOLDS, W. C. & HUSSAIN, A. K. M. F. 1972 The mechanics of an organized wave in turbulent shear flow. Part 3. Theoretical models and comparisons with experiments. *J. Fluid Mech.* **54**, 263–288.

ROSENBERG, B. J., BUREN, T. V., FU, M. K. & SMITS, A. J. 2016 Turbulent drag reduction over air- and liquid-impregnated surfaces. *Phys. Fluids* **28**, 015103.

ROTHSTEIN, J. P. 2010 Slip on superhydrophobic surfaces. *Annu. Rev. Fluid Mech.* **42**, 89–109.

SCHÖNECKER, C., BAIER, T. & HARDT, S. 2014 Influence of the enclosed fluid on the flow over a microstructured surface in the Cassie state. *J. Fluid Mech.* **740**, 168–195.

SEO, J., GARCÍA-MAYORAL, R. & MANI, A. 2015 Pressure fluctuations and interfacial robustness in turbulent flows over superhydrophobic surfaces. *J. Fluid Mech.* **783**, 448–473.

SEO, J. & MANI, A. 2016 On the scaling of the slip velocity in turbulent flows over superhydrophobic surfaces. *Phys. Fluids* **28**, 025110.

SEO, J. & MANI, A. 2017 Effect of texture randomization on the slip and interfacial robustness in turbulent flows over superhydrophobic surfaces. *Preprint*, arXiv:1709.05605.

SQUIRE, H. B. 1953 Investigation of the instability of a moving liquid film. *Brit. J. Appl. Phys.* **4**, 167–169.

SRINIVASAN, S., KLEINGARTNER, J. A., GILBERT, J. B., COHEN, R. E., MILNE, A. J. B. & MCKINLEY, G. H. 2015 Sustainable drag reduction in turbulent Taylor–Couette flows by depositing sprayable superhydrophobic surfaces. *Phys. Rev. Lett.* **114**, 014501.

STEINBERGER, A., COTTIN-BIZONNE, C., KLEIMANN, P. & CHARLAIX, E. 2007 High friction on a bubble mattress. *Nat. Mater.* **6**, 665–668.

TAYLOR, G. I. 1959 The dynamics of thin sheets of fluid. ii. Waves on fluid sheets. *Proc. R. Soc. Lond.* A **253**, 296–312.

TEO, C. J. & KHOO, B. C. 2010 Flow past superhydrophobic surfaces containing longitudinal grooves: effects of interface curvature. *Microfluid. Nanofluid.* **9**, 499–511.

TEO, C. J. & KHOO, B. C. 2014 Effects of interface curvature on Poiseuille flow through microchannels and microtubes containing superhydrophobic surfaces with transverse grooves and ribs. *Microfluid. Nanofluid.* **16**, 225–236.

TSAI, P., PETERS, A. M., PIRAT, C., WESSLING, M., LAMMERTINK, R. G. H. & LOHSE, D. 2009 Quantifying effective slip length over micropatterned hydrophobic surfaces. *Phys. Fluids* **21**, 112002.

TÜRK, S., DASCHIEL, G., STROH, A., HASEGAWA, Y. & FROHNAPFEL, B. 2014 Turbulent flow over superhydrophobic surfaces with streamwise grooves. *J. Fluid Mech.* **747**, 186–217.

WENZEL, R. N. 1936 Resistance of solid surfaces to wetting by water. *Ind. Engng Chem.* **28**, 988–994.

WEXLER, J. S., GROSSKOPF, A., CHOW, M., FAN, Y., JACOBI, I. & STONE, H. A. 2015*a* Robust liquid-infused surfaces through patterned wettability. *Soft Matt.* **11**, 5023–5029.

WEXLER, J. S., JACOBI, I. & STONE, H. A. 2015*b* Shear-driven failure of liquid-infused surfaces. *Phys. Rev. Lett.* **114**, 168301.

WOOLFORD, B., PRINCE, J., MAYNES, D. & WEBB, B. W. 2009 Partical image velocimetry chracterization of turbulent channel flow with rib patterned superhydrophobic walls. *Phys. Fluids* **21**, 085106.

XUE, Y., LV, P., LIU, Y., SHI, Y., LIN, H. & DUAN, H. 2015 Morphology of gas cavities on patterned hydrophobic surfaces under reduced pressure. *Phys. Fluids* **27**, 092003.

YBERT, C., BARENTIN, C. & COTTIN-BIZONNE, C. 2007 Achieving large slip with superhydrophobic surfaces: scaling laws for generic geometries. *Phys. Fluids* **19**, 123601.

ZHANG, J., TIAN, H., YAO, Z., HAO, P. & JIANG, N. 2015 Mechanisms of drag reduction of superhydrophobic surfaces in a turbulent boundary layer flow. *Exp. Fluids* **56**, 179.